Bone 131 (2020) 115111

Contents lists available at ScienceDirect

Bone

journal homepage: www.elsevier.com/locate/bone

Full length article

Reduction of fibrillar strain-rate sensitivity in steroid-induced osteoporosis linked to changes in mineralized fibrillar nanostructure

L. Xi[a,b,1], P. De Falco[b,c,1], E. Barbieri[b,d], A. Karunaratne[e], L. Bentley[f], C.T. Esapa[f,g], G.R. Davis[l], N.J. Terrill[h], R.D. Cox[f], N.M. Pugno[i,b,j], R.V. Thakker[g], R. Weinkamer[c], W.W. Wu[a,*], D.N. Fang[a,k], H.S. Gupta[b,**]

[a] Institute of Advanced Structure Technology, Beijing Institute of Technology, Beijing 100081, China
[b] School of Engineering and Material Sciences, Queen Mary University of London, London, E1 4NS, UK
[c] Department of Biomaterials, Max Planck Institute of Colloids and Interfaces, D-14424 Potsdam-Golm, Germany
[d] Department of Mathematical Science and Advanced Technology (MAT), Yokohama Institute for Earth Sciences (YES) 3173-25, Showa-machi, Kanazawa-ku, Yokohama-city, Japan
[e] Department of Mechanical Engineering, University of Moratuwa, Sri Lanka
[f] MRC Mammalian Genetics Unit and Mary Lyon Centre, MRC Harwell, Harwell Science and Innovation Campus, OX11 0RD, UK
[g] Academic Endocrine Unit, Radcliffe Department of Clinical Medicine, Oxford Centre for Diabetes, Endocrinology and Metabolism (OCDEM), University of Oxford, Churchill Hospital, Headington, Oxford, OX3 7JL, UK
[h] Beamline I22, Diamond Light Source Ltd., Diamond House, Harwell Science and Innovation Campus, Chilton, Didcot, Oxfordshire, OX11 0DE, United Kingdom
[i] Laboratory of Bio-Inspired & Graphene Nanomechanics, Department of Civil, Environmental and Mechanical Engineering, University of Trento, Via Mesiano, 77, 38123, Trento, Italy
[j] Ket Lab, Edoardo Amaldi Foundation, Via del Politecnico snc, 00133, Rome, Italy
[k] State Key Laboratory for Turbulence and Complex Systems, College of Engineering, Peking University, Beijing, China
[l] Dental Physical Sciences Unit, Queen Mary University of London, London, E1 4NS, UK

ARTICLE INFO

Keywords:
Glucocorticoid induced osteoporosis
Synchrotron X-ray nanomechanical imaging
Nanoscale deformation mechanisms
Multiscale Mechanical modelling

ABSTRACT

As bone is used in a dynamic mechanical environment, understanding the structural origins of its time-dependent mechanical behaviour – and the alterations in metabolic bone disease – is of interest. However, at the scale of the mineralized fibrillar matrix (nanometre-level), the nature of the strain-rate dependent mechanics is incompletely understood. Here, we investigate the fibrillar- and mineral-deformation behaviour in a murine model of Cushing's syndrome, used to understand steroid induced osteoporosis, using synchrotron small- and wide-angle scattering/diffraction combined with *in situ* tensile testing at three strain rates ranging from 10^{-4} to 10^{-1} s^{-1}. We find that the effective fibril- and mineral-modulus and fibrillar-reorientation show no significant increase with strain-rate in osteoporotic bone, but increase significantly in normal (wild-type) bone. By applying a fibril-lamellar two-level structural model of bone matrix deformation to fit the results, we obtain indications that altered collagen-mineral interactions at the nanoscale – along with altered fibrillar orientation distributions – may be the underlying reason for this altered strain-rate sensitivity. Our results suggest that an altered strain-rate sensitivity of the bone matrix in osteoporosis may be one of the contributing factors to reduced mechanical competence in such metabolic bone disorders, and that increasing this sensitivity may improve biomechanical performance.

* Corresponding author.
** Correspondence author at: School of Engineering and Materials Sciences and Institute of Bioengineering, Queen Mary University of London, Mile End Road, London E1 4NS, UK.
E-mail addresses: xili@bit.edu.cn (L. Xi), paolino.defalco@mpikg.mpg.de (P. De Falco), e.barbieri@jamstec.go.jp (E. Barbieri), angelok@uom.lk (A. Karunaratne), l.bentley@har.mrc.ac.uk (L. Bentley), c.esapa@har.mrc.ac.uk (C.T. Esapa), g.r.davis@qmul.ac.uk (G.R. Davis), r.cox@har.mrc.ac.uk (R.D. Cox), nicola.pugno@unitn.it (N.M. Pugno), rajesh.thakker@ndm.ox.ac.uk (R.V. Thakker), richard.weinkamer@mpikg.mpg.de (R. Weinkamer), wuwenwang@bit.edu.cn (W.W. Wu), fangdn@bit.edu.cn (D.N. Fang), h.gupta@qmul.ac.uk (H.S. Gupta).
[1] These authors contributed equally to this work.

https://doi.org/10.1016/j.bone.2019.115111
Received 16 July 2019; Received in revised form 13 October 2019; Accepted 15 October 2019
Available online 11 November 2019

1. Introduction

Determining the mechanically-critical structural and compositional alterations of bone matrix in metabolic bone disorders, such as osteoporosis or osteogenesis imperfecta, is essential to understand origins of the reduced mechanical competence exhibited in such disorders [1–3]. A systematic characterization of the mechanical properties of bone was pioneered by John Currey [4]. Among his many contributions to biomechanics, he found that stiffness, strength and toughness of bone depend on biological factors such as anatomical specialisation [5] and species [6], as well as on factors related to materials-composition and structure, such as mineral [7] and collagen content [8,9]. The research presented here was performed in the spirit of his systematic approach, but focusses not on quasi-static mechanical properties, but on changes of the mechanical performance under three different loading speeds. As bone is used under time-dependent loading in a dynamic mechanical environment, linking the viscoelastic and strain-rate dependent behaviour of bone matrix to such alterations is important. However, clinical measures assessing bone state (such as bone mineral density (BMD)) capture mainly changes in bone mass, and provide little information on alterations in quality of the bone matrix. The matrix of bone at the nanoscale is a composite of Type-I collagen fibrils, carbonated apatite, noncollageneous proteins and water [10,11], which are assembled into fibre-arrays at the micron-scale [12,13] and further aggregate into trabecular and cortical bone types to form the organ bone [5]. Metabolic bone diseases may affect not only the macro- and microscale structure of bone, but also change the bone matrix-level quality [2], via altered cellular modelling and remodelling cycles. Alterations in matrix quality, such as collagen-cross linking [8,9,14] mineral-platelet structural changes [15] and the expression of noncollageneous proteins like osteopontin [16], have been shown to lead to deterioration or alteration in macroscopic mechanical properties, but the details of the nanoscale mechanisms are not completely understood. Understanding the nanostructural response of bone matrix to time-dependent loading in bone-disease types like osteoporosis is therefore of importance both to basic medical science as well as, eventually, to clinical practice.

In this regard, glucocorticoid induced osteoporosis (GIOP) is a prototypical secondary osteoporosis where BMD is known to be insufficient to explain mechanical changes. As the most common form of secondary osteoporosis, GIOP affects 1–3% of the general population and results in severe morbidity, especially in post-menopausal women and older men [17,18]. GIOP usually develops in patients receiving glucocorticoids for the treatment of a variety of diseases like inflammatory and autoimmune disorders, and these underlying diseases themselves can also have negative effects on bone metabolism which constitute a risk of osteoporosis [19]. Glucocorticoids treatment results in altered bone remodelling, early and rapid bone loss and increased fracture risk, through direct effects on bone cells and indirect effects through alteration of the neuromuscular system and gonadal hormones [20]. As a crucial process in GIOP, reduced bone volume is caused by osteoclastic activity (bone resorption) that cannot be matched by osteoblastic activity (bone formation) [21,22]. Glucocorticoids suppress bone formation through inducing osteoblast and osteocyte apoptosis and the inhibition of proliferation, differentiation, maturation and activity of osteoblasts [23]. In the presence of glucocorticoids, the osteoblast precursor cells (mesenchymal cells) in bone marrow are not differentiated or directed toward osteoblastogenesis, but toward adipogenesis (cells of the adipocytic lineage) [24]. Glucocorticoids inhibit the differentiation of osteoblasts by a mechanism of opposing *Wnt/β*-catenin pathway, and *Wnt* signalling plays a critical role in increasing bone mass through induction of differentiation of bone-forming cells (osteoblasts), inhibition of osteoblast and osteocyte apoptosis, and suppression of the development of bone-resorbing cells (osteoclasts) [25,26]. Glucocorticoids directly affect osteoclasts resulting in decreased osteoclast apoptosis and increased osteoclast formation of a prolonged life span, which explains the observed enhanced and prolonged bone resorption [27]. The proliferation of osteoclasts is inhibited by glucocorticoids in a dose dependent manner. Although excess of glucocorticoids leads to an increased osteoclast number, osteoclast function may be affected too, with impaired spreading and resorption of mineralized matrix. The osteoblast signals could also be impaired due to the abnormal osteoclast function [28].

However, the way these biological changes in GIOP affect the nano- and microscale mechanics is incompletely understood, especially in the area of time-dependent loading. Previous studies have showed that glucocorticoid therapy affects not only the amount of bone (bone quantity) but also the micro-architecture and other material level properties (bone quality) [17,29,30]. Micro-CT studies of trabecular and cortical bone with glucocorticoids treatment showed reduced trabecular bone volume, trabecular connectivity, trabecular number and cortical thickness as compared to control group [31,32]. Glucocorticoid-treated mice showed increased size of osteocyte lacunae and there are “halos” of hypomineralized bone surrounding the lacunae, with corresponding reduced (~ 40 %) mineral to matrix ratio as measured by Raman microspectroscopy. A reduction in mineral concentration (by 45 %) caused by glucocorticoids treatment is accompanied by reduced degree of bone mineralization, as compared to controls [31]. Our previous study on a mouse model of endogenous hypercorticosteronaemia (Cushing's syndrome) shows a significant reduction (by 51 %) of fibril modulus, larger fibril strain/tissue strain ratio and a disruption of intracortical architecture as compared with their wild-type littermates [33]. In relation to mechanics, bone fractures in healthy individuals usually happen with traumatic events at high strain rates, whereas in GIOP, bones are additionally involving fragility fractures with minimal trauma at relatively low strain rates [1,34,35]. Since the quasi-static fibrillar-level mechanics and structure are altered in GIOP-bone [15,33], it is therefore of interest to investigate, in this prototypical secondary osteoporosis, possible viscoelastic and strain-rate dependent effects in the mineralized fibrillar matrix.

In this study, we examine the deformation of the mineralized fibrils in the bone matrix of a GIOP mouse model at three different strain rates, using high-brilliance time-resolved synchrotron small-angle X-ray scattering (SAXS) and wide-angle X-ray diffraction (WAXD). These X-ray techniques provide information on the fibrillar- and mineral platelet-level strain in the bone matrix, induced by external mechanical loads. When combined with a high brilliance synchrotron source, SAXS/WAXD measurements can be carried out with time-resolution of the order of seconds [14,15,36–38], facilitating dynamic measurements. For the animal model of GIOP, we use a mouse model ($Crh^{-120/+}$) of endogenous hypercorticosteronaemia (Cushing's syndrome), published as a model of endogenous GIOP [39]. Prior work has suggested that fracture risk in endogenous glucocorticoid production (Cushing’s syndrome) is similar to that in exogenous GIOP [40], although we acknowledge of the limitation of using mouse models to understand human GIOP, due to the absence of secondary osteonal remodelling. Our previous quasi-static (not time-dependent) SAXS/WAXD study, on the developmental changes in bone nanostructure in this model, provided evidence for increased fibrillar deformability, more random fibrillar orientation, and shorter/less stress-reinforcing mineral platelets in GIOP [15,33]. Here, we carry out tensile deformation on cortical GIOP mouse bone at a fixed age point (24 weeks) and at three strain rates to quantify the alterations in fibrillar mechanics in comparison to wild-type animals. Because SAXS/WAXD measurements are intrinsically volume-averaged measures of nanoscale deformation, the experimental data is combined with a multiscale model of the mechanics of the fibrils and fibril-arrays, developed from previous work [13,36,41], to help in the interpretation of the experimental results.

2. Materials and methods

2.1. Animals

Bone tissue from female GIOP mice ($Crh^{-120/+}$) and wild-type ($Crh^{+/+}$) littermates on a C57BL/6 genetic background (3rd generation) aged 24 weeks were used in this study. Mouse samples were stored at −20 °C before experiments. The mice were bred as part of a prior study [39], where all animal studies were carried out using guidelines issued by the UK Medical Research Council, in Responsibility in Use of Animals for Medical Research (July 1993) and Home Office Project License numbers 30/2433 and 30/2642.

2.2. Sample preparation for in situ tensile testing

Murine femora were dissected and longitudinally sectioned along the long axis using a water-irrigated low speed saw with a diamond-coated blade. The distal and proximal ends of anterior femora strips were embedded in dental ionomer (FiltekTM Supreme XT, 3 M ESPE, USA) such that samples could be mounted in the microtensile tester. The dental ionomer was exposed in UV light for 20 s, while the mid-diaphysis of femora bone was covered by lead tap during UV light exposure to prevent any UV-induced tissue alteration. The obtained femora strips for microtensile testing have typical gauge length, width and thickness of 5 mm, 1 mm and 0.2 mm, respectively. Samples were then wrapped in PBS-soaked tissue paper and stored at - 20 °C before used for mechanical testing.

2.3. In situ micro tensile testing with simultaneous synchrotron SAXD/WAXD measurements

Combining *in situ* tensile testing with real time synchrotron SAXD and WAXD, the load data (from load cell), fibril strain ε_f (from the SAXD frames) and mineral strain ε_m (from the WAXD frames) can be collected concurrently, as initially devised by Gupta et al. [37]. A customized microtensile tester was mounted in the path of synchrotron X-ray beam at beamline I22, Diamond Light Source (Harwell, UK), such that SAXD and WAXD frames were collected concurrently with mechanical loading of the sample. Samples were uniaxially loaded in tension using a customized microtensile tester equipped with a DC linear-encoder stage (M112.1DG; Physic Instruments, UK) and an 111 N model SLC31/00025 tension/compression load cell (RDP Electronics Ltd, UK). A custom LabVIEW based software (LabVIEW 2013, National Instruments, UK) was used to control the microtensile tester and CCD camera. Samples were tested at room temperature and hydrated throughout each experiment in a fluid bath filled with physiological saline (PBS solution).

For the three different load rates used in the current study, the motor velocities were set to be 0.1, 0.05 and 0.002 mm/s, which corresponding to motor strain rates of 0.02 s^{-1}, 0.01 s^{-1} and 0.0004 s^{-1}, respectively. Strain rates of 0.02 s^{-1} and 0.01 s^{-1} were used because they are in the range of physiological strain rates during walking and running, whereas a strain rate of 0.0004 s^{-1} representing the quasi-static loading was also examined as strain rates near this magnitude have been used in our previous studies [15,33,42,43]. The numbers of samples tested at strain rate of 0.02 s^{-1}, 0.01 s^{-1} and 0.0004 s^{-1} were 4, 4 and 4, respectively, for wild-type mice; and 6, 5 and 4, respectively, for GIOP mice.

For the synchrotron SAXD and WAXD measurement, the X-ray wavelength λ was 0.8857 Å and beam cross section was ~240 × 80 μm at the sample. A Pilatus P3 − 2 M detector was used to collect the SAXD data, while a Pilatus P3-2M-DLS-L detector was used to collect the WAXD data; both detectors have a pixel resolution of 1475 × 1679 pixels and pixel size of 172 × 172 μm^2. Note that in the concurrent SAXD/WAXD measurement protocol used, one quadrant (lower right) of the WAXD detector space is removed to allow for the remaining SAXD signal to transmit to the downstream SAXD detector; as a result, the WAXD pattern spans 3 out of 4 quadrants on the detector. The sample-to-detector distance was ~ 3727.0 mm for SAXD detector and ~ 175.3 mm for WAXD detector, as measured with Silver Behenate and Silicon standard, respectively. The X-ray exposure time was 0.1 s for both SAXD and WAXD patterns for samples measured at all strain rates. Due to the different durations of the mechanical tests at different strain-rates, the period between successive SAXD/WAXD acquisitions (with beam shutter closed) was controlled by the wait-time parameter (0.1 s: strain rate 0.01 s^{-1} and 0.02 s^{-1}, and 3.4 s: strain rate of 0.0004 s^{-1}). The beam shutter was closed between consecutive acquisitions of SAXD and WAXD patterns, to minimise the effect of X-ray irradiation on the mechanical properties of bone tissue [44].

2.4. SAXD and WAXD data analysis

Fibril strains and load-induced changes in fibrillar orientation distribution were measured from 2D SAXD patterns, and mineral strains were measured from 2D WAXD patterns.

2.4.1. Fibril strain

The meridional stagger (D-period) of collagen molecules inside the fibril leads to an axial diffraction pattern in the small-angle region of reciprocal space [45]. The third-order meridional collagen reflections were used to measure the D-period of collagen fibrils evaluating a radially-narrow semi-circular sector (180° angular width) (Fig. 1G); this corresponds to considering an integrated averaged of fibrillar deformation in all directions. The fibril strain (ε_f) was calculated from the percentage increases in D-period during tensile testing of samples [15,33,45,46]. SAXD patterns at different stress levels are shown in the Supplementary Information (Figure S1).

2.4.2. Mineral strain

For WAXD, the mineral particles consist of apatite (with a lattice structure of hexagonal closed-packed or *hcp* type) with the *c*-axis predominantly oriented along the fibril direction [47]. In a similar manner to the SAXD analysis, the mineral strain (ε_m) along the loading direction was measured from the percentage changes of lattice spacing, obtained from the (002) peak centre position of apatite averaged in a radially-narrow semi-circular (180° angular width) in the upper quadrant, in an analogous manner to SAXD (Fig. 1E), similar to prior work [14,15,38,45].

The *Processing* perspective of the data analysis software package DAWN [48] (www.dawnsci.org) was used for SAXD and WAXD data reduction. The integrated SAXD and WAXD 1D intensity profiles (Fig. 1F and H) were obtained from 2D SAXS/WAXD images as described above. Subsequently, the 1D profiles were fitted using a custom Python script. Both the 1D collagen SAXD data and the 1D mineral WAXD data were fitted to combinations of a Gaussian peak and a linear background term. To analyse the change of fibril and mineral strains during tensile loading, the obtained peak centre positions were used to calculate the D-period for the collagen fibrils and the (002) crystallographic lattice spacing for the mineral apatite. Linear regressions of D-period and D(002) were carried out versus macroscopic stress, and the intercept of each regression was taken as the unstrained (zero-stress) value for D-period and D(002). The collagen fibril strains ε_f and mineral strains ε_m were calculated from the percentage changes of collagen D-period and the (002) lattice spacing, respectively, relative to the unstrained state. The *effective fibril modulus* ($E_f = d\sigma/d\varepsilon_f$) and *effective mineral modulus* ($E_m = d\sigma/d\varepsilon_m$) were defined as the slope of tissue-level stress σ versus fibril strain and mineral strain, respectively, from the elastic region of deformation (Fig. S3 and 4, Supplementary Information), as described in prior work [15,33,45]. We note that the terminology (effective fibril modulus and mineral modulus) is used for consistency with prior work [15,33,49], and as will be discussed in the modelling section, these parameters are not equivalent to the actual

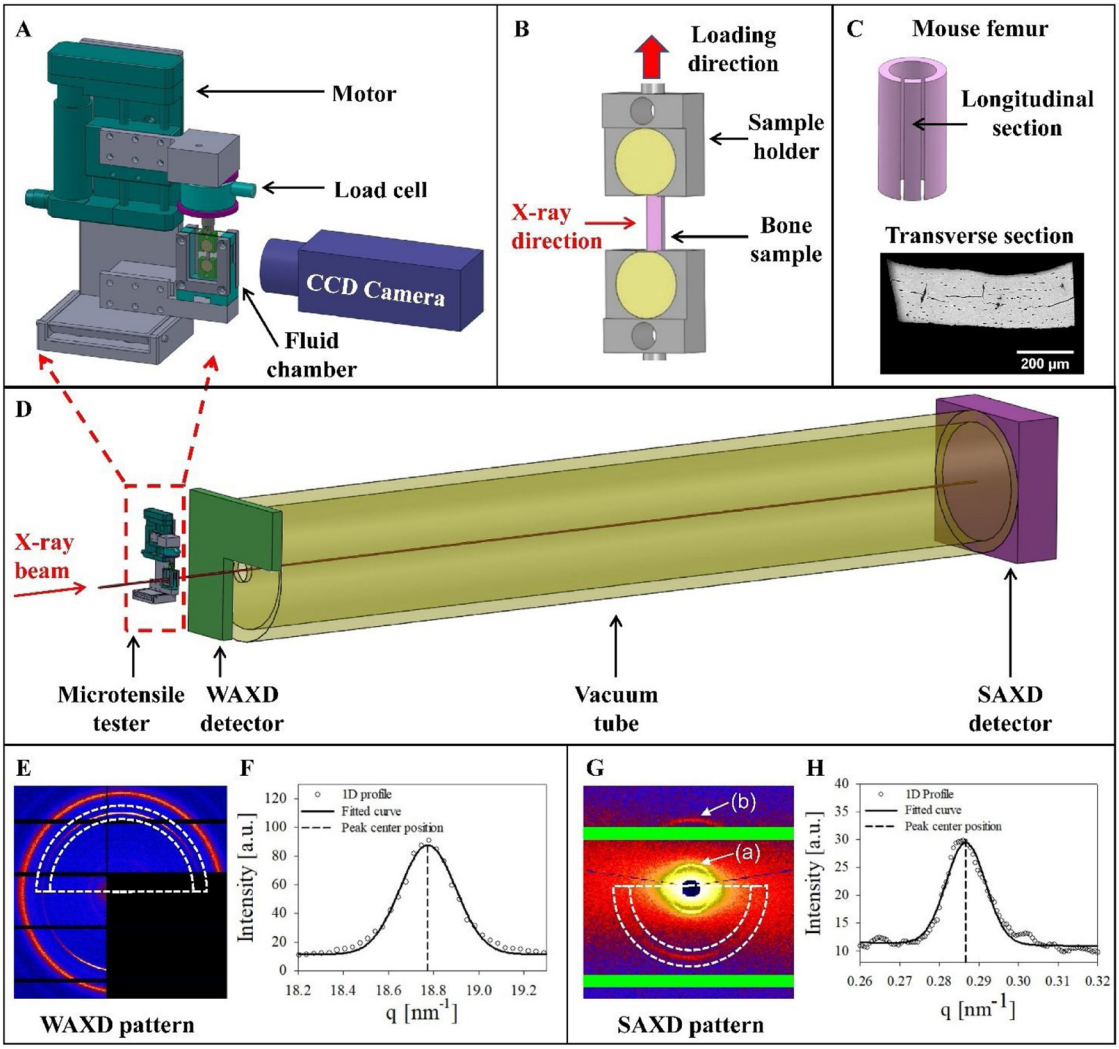

Fig. 1. In situ nanomechanics with simultaneous synchrotron SAXD and WAXD.
(A) Customized tensile tester with bone sample mounted in a fluid chamber. (B) Magnified view of sample and tensile grips in fluid chamber, with tensile strain along the vertical direction. (C) Upper: Schematic of mouse femur, with tensile test specimen sectioned along the long axis of femur; lower: backscattered electron image of transverse section of specimen. (D) Experimental configuration: Tensile tester with specimen mounted along the X-ray beam path in transmission geometry; an L-shape WAXD detector, vacuum tube and SAXD detector were positioned along the X-ray beam path. (E) 2D WAXD pattern from bone apatite with predominant c-axis orientation vertical. Dotted lines denote the 180° region for azimuthal averaging of intensity around the (002) peak of apatite. (F) Azimuthally averaged radial intensity profile I(q) for the pattern in E. (G) 2D SAXD pattern from collagen fibrils in bone with predominant fibril orientation vertical. Dotted lines denote the 180° region over which the collagen reflection is averaged azimuthally; (a) the first-order and (b) the third-order collagen reflection. (H) Azimuthally averaged radial intensity profile I(q) for the pattern in G. For F and H, black solid line: peak fit with a Gaussian function plus a linear baseline; black dashed line: peak centre position.

fibril and mineral elastic modulus (hence the use of the qualifier "effective").

2.4.3. Fibrillar orientation distribution

The changes in fibrillar orientation distribution with tensile load were analysed by observing the narrowing of the FWHM of the angular variation of SAXD intensity of the first-order collagen reflection, as described in our prior study on quasi-static deformation of glucocorticoid-induced osteoporotic bone [33]. Using the DAWN processing perspective, radially averaged azimuthal intensity profiles $I(\chi; q_0)$ were calculated over the full azimuthal range (360°) from the first-order collagen reflection (at $q = q_0 = 6\pi/D$). To subtract out the diffuse scattering background due to the mineral, similar azimuthal intensity profiles $I_m(\chi; q_0-\Delta q)$ and $I_m(\chi; q_0+\Delta q)$ near the first-order collagen reflection, with $\Delta q = 0.015\ nm^{-1}$ chosen to have $q_0 \pm \Delta q$ outside of the first-order collagen peak, were calculated and averaged. The corrected azimuthal intensity profile $I_c(\chi)$ was calculated as $I_c(\chi) = I(\chi; q_0) - 0.5\times [I_m(\chi; q_0-\Delta q) + I_m(\chi; q_0+\Delta q)]$. The obtained $I_c(\chi)$ was fitted with a pair of Gaussian peak functions separated by 180°. From the fit, the peak position indicates the predominant direction of fibril orientation, while the peak width (FWHM) is related to the extent of fibrillar alignment: larger FWHMs correspond to lower alignment (See Fig. S2 in the Supplementary Information). The rate of fibrillar reorientation was calculated from the slope of FWHM (degrees) versus fibril strain (%) curve for each sample [33], with units of degrees/%.

2.5. X-ray microtomography

X-ray microtomography was used to study 3D micromorphometry and microscale mineralization distribution of bone tissue. Mice femora were longitudinally sectioned into two halves. Five samples from both wild-type and GIOP mice were used for X-ray microtomography measurements to obtain tomograms, which were used for quantitative analysis of microscale mineralization distribution in femoral mid-shaft from both wild-type and GIOP mice. Samples were mounted on the sample stage of a high-definition X-ray microtomography scanner

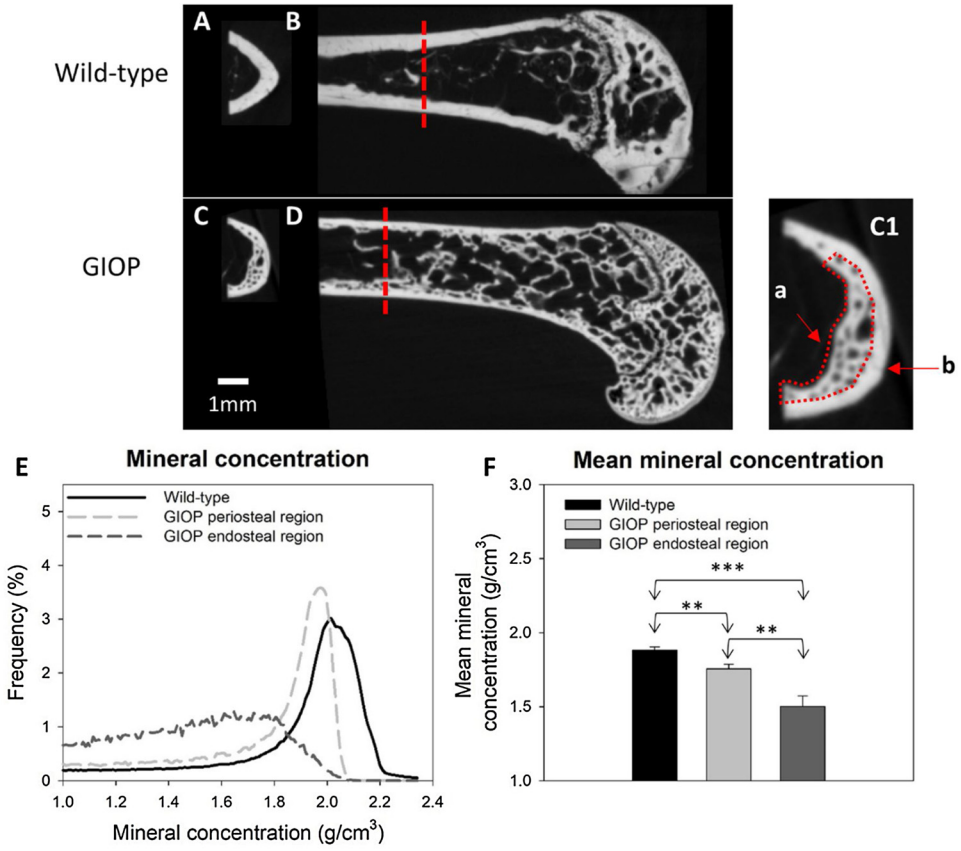

Fig. 2. X-ray microtomography and degree of mineralisation.
Representative 2D slices from X-ray microtomography measurement for both transverse (A, C) and longitudinal (B, D) cross sections of femora from wild-type and GIOP mice. Red dash line indicated location where the 2D slice of transverse cross section was taken. C1: Inset on right shows an example 2D transverse slice, with (a) indicating the endosteal region and (b) the periosteal region. (E) Representative histograms of degree of mineralisation were plotted for wild-type (black), GIOP periosteal regions (light gray) and GIOP endosteal regions (dark gray). (F) Bar chart of the mean mineral concentration for wild-type cortex, GIOP periosteal regions and GIOP endosteal regions. Error bars shown are standard deviations. Statistical significances were denoted on the figures (*p < 0.05, **p < 0.01, ***p < 0.001, ns: not significant).

(MuCat scanner) which equipped with an ultrafocus X-ray generator (Nikon Metrology (Leuven, Belgium)) and CCD camera (Spectral Instruments Inc (Tucson, Arizona, USA)) in a time-delay integration readout mode. An accelerating voltage of 40 kV was used to scan mice femora samples and a voxel size of 15 × 15 × 15 μm^3 was obtained. The projection data were processed following a calibration procedure, in which the scanning data were corrected to an equivalence of 25 keV monochromatic X-ray source, and then a reconstruction procedure in which a cone-beam back-projection algorithm was used to generate 3D images (representing the absolute linear attenuation coefficient at 25 keV) of the scanned regions of samples. The 3D tomograms of samples were processed with an in-house software (Tomview, authored by GRD) to export a series of 8-bit grey level slices, multiplying the linear attenuation coefficient by a known constant to obtain an appropriate dynamic range. The histograms of grey levels for wild-type mice and two distinct regions of interest in GIOP mice - periosteal region and endosteal region (Fig. 2C1)- were generated from 2D slices using ImageJ software (ImageJ, NIH, USA). The histograms of grey levels for three data groups were converted into histograms of mineral concentration using published X-ray attenuation data [50], from which the average mineral concentrations (denoted as the degree of mineralisation) measured as hydroxyapatite (g/cm^3) were calculated and plotted for different bone regions (Fig. 2E and F). The mineral concentration is converted to mineral volume fraction as previously described [51,52]. For input of experimental mineral concentrations into the model (described below), the mineral concentration and volume fraction are taken as the average values across the cross-section of the tissue, similar to our prior work [15].

2.6. Calculation of microscale porosity and stress

The experimental stress data was calculated by the load values divided by the area of the fracture surface, and then corrected by the porosity of bone, following our previous study [15]. SEM image was taken on the fracture surface while the fractured sample was mounted vertically, and the area of the fracture surface was measured from SEM image using ImageJ (NIH, Bethesda, USA). The experimental stress data were post-multiplied by the coefficient $1/(1 - p^{3/2})$ to incorporate the effects – on the effective cross-sectional area – of a 3D isotropic distribution of internal porosity in bone [15]. In this case the 3D porosity is $p^{3/2}$, where p is the 2D porosity coefficient (p = 2D area of voids / 2D bone cross section area), as analysed from backscattered electron (BSE) imaging of the cross section of femoral mid-diaphysis of wild-type and GIOP bone, following our earlier work (Supplementary Information in [15]).

2.7. Statistical analysis

To test for statistical differences in bone mineralization and the nanoscale mechanical deformation behaviour between samples tested at three different strain-rates, one-way ANOVA tests with all pairwise multiple comparison procedures (Holm-Sidak method) were performed on the experimental measured results including the mean mineral concentration, the effective fibril modulus, the effective mineral modulus and the fibrillar reorientation rate. SigmaPlot (Systat Software Inc., USA) was used for the statistical analysis. The statistical significances were denoted on the figures (*: $p < 0.05$, **: $p < 0.01$, ***: $p < 0.001$, ns: not significant for $p > 0.05$).

2.8. Modelling of fibrillar and lamellar mechanics

To understand the structural mechanisms underpinning trends in E_f, E_m and fibrillar reorientation with strain-rate, we develop a two-level hierarchical model of the fibrils and fibril arrays, based on prior work, which is briefly summarized below (details in Supplementary Information). Analytical fitting (performed in *Matlab* [53]) and

Table 1
Description of the moduli introduced for the study of the bone mechanical properties at different length scales and of the fibrillar reorientation phenomenon. The term 'effective' indicates that the moduli result from the ratio of terms computed at different length scales. Specifically, they are calculated from the ratio of stresses applied at the macroscale and of strains computed at the microscale (effective fibril modulus) and at the nanoscale (effective mineral modulus). The equations used for the analytical calculation of these parameters are listed in Supplementary Information, Equations S1-S6. 'afs' is the average fibril strain, φ_{EM} is the volume fraction of the extrafibrillar matrix and k is a factor defined in Equation S6.

Nomenclature of the modulus	Experimental	Analytical/Numerical
Effective fibril modulus	$\frac{\text{Applied tissue stress}}{\text{average fibril strain}}$ Calculated via linear fitting of experimental data shown in Fig. 5A.	$\frac{\text{Applied laminate stress}}{\text{average strain of the sublamellae}}$ Computed via laminate theory.
Effective mineral modulus	$\frac{\text{Applied tissue stress}}{\text{mineral strain}}$ Calculated via linear fitting of experimental data shown in Fig. 5B.	$\frac{\text{Applied tissue stress}}{(afs * \varphi_{EM}) + (afs * \frac{(1-\varphi_{EM})}{k})}$ Computed via laminate theory.
ΔFWHM/fibril strain	ΔFWHM: variation of the FWHM of Gaussian fitting 'I vs χ' curves (more details in Supplementary Information). Fibril strain: average fibril strain, averaged from the volume of bone (beam size * sample thickness) measured by x-ray.	ΔFWHM: variation of the FWHM of the lamellar angular distribution (Gaussian distribution). The fibrillar reorientation leading to this variation was computed via FE simulations. Fibril strain: average strain of the sub-lamellae (computed via laminate theory).

numerical (finite element) simulations performed in *Abaqus 6.14* [54] are used to fit the model to data. The experimental parameters are fitted to equivalent model parameters, summarized in the two columns of Table 1.

2.9. Model structure and parameters

2.9.1. Analytical relations

2.9.1.1. Nanoscale force-balance relations. Stresses and strains on the fibril, mineral platelet and extrafibrillar matrix were calculated by considering the fibril as a staggered array of mineral particles embedded with a collagen matrix (Fig. 3A–I), which is in turn embedded in an extrafibrillar matrix. The model follows earlier work on staggered model architecture of the mineralized fibrils in bone and related biomineralized tissues [11,36,41,55–57]. The mineral platelet aspect ratio was taken as 15 and 9.6 respectively for the wild-type and GIOP models, following our prior ultrastructural determination of mineral structure (*L*-parameter) using WAXD on GIOP- and WT-bone from the same cohort at a similar age-point [15]. A second parameter of note in the staggered model is the *k*-factor, which is inversely related to the stress transferred to the mineral via shear in the collagen matrix [11,36]. Mineral and collagen were taken as elastic, and the strain-rate sensitivity was incorporated into the material response of the extrafibrillar matrix, whose constitutive law was taken as the Ramberg-Osgood law $\varepsilon = \sigma/(c\dot{\varepsilon}^d)$ [58,59]. Most parameters were obtained from referenced literature (Table 2), with the exception of the Young's modulus and volume fraction of the extrafibrillar matrix, and the *k*-factor, which are obtained from nonlinear fitting to the experimental data (Fig. S6) and will be reported in the Results. The tissue mineral volume fraction values were taken from the 24-week time-point values of volume fraction in GIOP- and WT-mice, in our recent work [15], with $\phi_m = 0.40$ for GIOP and $\phi_m = 0.45$ for WT.

2.9.1.2. Plywood structural parameters. The bone lamella was modelled as a set of differently oriented fibril layers, with angular orientations at 0°, ± 5°, ± 10°, ± 15°, ± 30°, ± 45°, ± 60°, ± 75° and 90°. To determine the relative thicknesses of each layer, these were varied till the FWHM of the simulated fibril orientation distribution matched the experimental azimuthal intensity distribution of the meridional collagen SAXD peak (Fig. S2), in a manner similar to our previous work [15]. Details are provided in Supplementary Information.

2.9.1.3. Matching to experimental data. Least-squares minimizations was carried out by simultaneously fitting the experimental E_f and E_m data to the model expressions (Fig. 5 and Fig. S6 in Supplementary Information). Each fitted experimental point (at a given strain rate) was weighted by the inverse of its squared standard deviation [60]. The weighted fitting process was performed in *Matlab* with the function *Nlinfit* [53] (Table 1 and implementation in Supplementary Information). Table 2 describes the choice of the input parameters for the model.

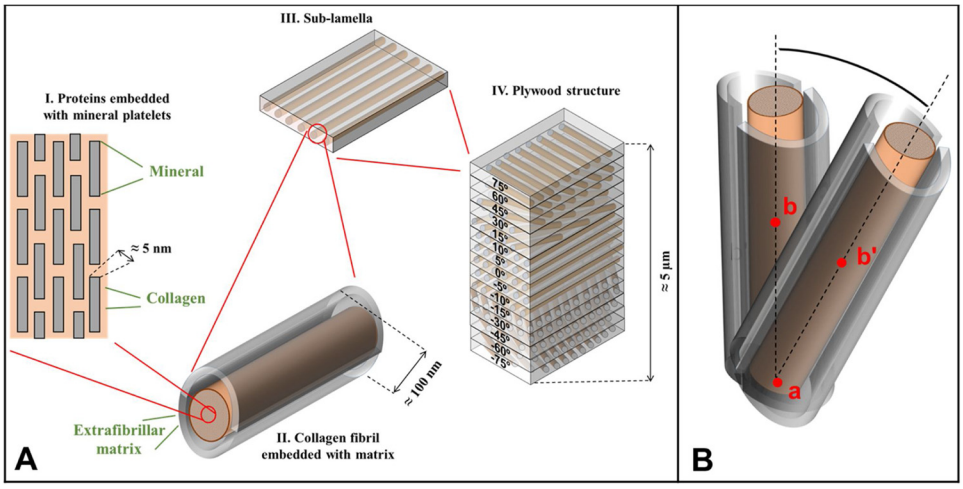

Fig. 3. Schematic of the hierarchical structure of bone assumed for the modelling approach. A) I. At the lowest hierarchical scale, a staggered arrangement of hydroxyapatite mineral platelets and collagen [41] (left side of the figure) was considered. The material components are collagen, hydroxyapatite mineral and extrafibrillar matrix (which together form level II). A bunch of parallel collagen fibrils surrounded by an extrafibrillar matrix, forming a sublamella (III). A set of sub-lamellae, each with the longitudinal axis of fibrils pointing toward a specific direction, forms (IV) a plywood (or Bouligand [79]) system. For both modelling approaches the scheme in Ref. [13] with an angular distribution of sub-lamellae of the type: 0°, +/-5°, +/-10°, +/-15°, +/-30°, +/-45°, +/- 60°, +/-75°, (0° direction is along the applied loads). B) Schematic for reorientation in the model.

Table 2
Elastic material properties of the basic components and their volume fractions in the Wild and GIOP models at low, medium and high strain rate values. Red: values extrapolated from referenced literature; Blue (with light blue background): values obtained from the fitting process; Black with dark grey background: values that were assumed. The k-factor is linked to the reinforcement of the collagen fibrils by the mineral platelets (Eqs. S2 and S6 in Supplementary Information) (for interpretation of the references to colour in this table legend, the reader is referred to the web version of this article).

Young's moduli	**GIOP bone (GPa)**	**Wild-type bone (GPa)**
E_c = Young's modulus of collagen	2.5 [36]	2.5 [36]
E_m = Young's modulus of hydroxyapatite (mineral content)	100 [36]	100 [36]
E_{EM} = Young's modulus of extrafibrillar matrix	k = 1.58 / k = 1.6 / k = 1.7 low s.r.: 163.8 / 107.6 / 53.0 medium s.r.: 160.8 / 105.7 / 52.3 high: 160.1 / 105.3 / 52.1	Extrafibrillar matrix low s.r.: 3.5 medium s.r.: 159.0 high: 370.0
Poisson's ratios		
ν_c = Poisson's ratio of collagen	0.3 [61]	0.3 [61]
ν_m = Poisson's ratio of hydroxyapatite (mineral content)	0.28 [61]	0.28 [61]
ν_{EM} = Poisson's ratio of extrafibrillar matrix	0.3 [61]	0.3
Volume fractions		
φ_c = volume fraction of collagen	0.6	0.55
φ_m = volume fraction of hydroxyapatite (mineral content)	k = 1.58: 0.37 / k = 1.6: 0.34 / k = 1.7: 0.27	0.45 - φ_{EM} = 0.37
φ_{EM} = volume fraction of extrafibrillar matrix	k = 1.58: 0.03 / k = 1.6: 0.06 / k = 1.7: 0.13	0.08 (from fitting)

2.9.2. Finite element simulations of fibrillar and lamellar reorientation

To simulate the load-induced reorientation of fibrils toward the loading axis, an approximate method was used, based on finite element simulations. The reorientation of a fibril embedded in an extrafibrillar matrix was determined (Fig. 3B), assuming isotropic material properties (**Table S2**), by applying a uniform traction of 10 MPa to the top edge of the fibril and calculating angular reorientation from the horizontal and longitudinal displacements. Details are provided in Supplementary Information.

3. Experimental results and model fitting

3.1. X-ray microtomography

X-ray microtomography was performed to investigate 3D micromorphometry, microscale mineralization distribution and possible mineralization defects of femora from wild-type and GIOP mice. A series of 8-bit grey level slices were obtained from the 3D tomograms of samples. Fig. 2 showed representative 2D slices for both longitudinal and transverse cross sections of femora from wild-type and GIOP mice. The 2D slices of transverse cross sections of femora, as shown in Fig. 2A and C, are selected from mid-shaft of mice femora as indicated by red dash lines in Fig. 2B and D. Clear qualitative differences can be observed in the cortical microstructure of GIOP mice as compare with wild-type mice. Both of the transverse and longitudinal cross sections of femoral from GIOP mice showed a very large fraction of cavities with less mineralized bone tissue near the endosteal cortex, whereas no such cavities were found in the femoral mid-shaft of wild-type mice. The femoral cross section of GIOP mice showed a much thinner cortex compared to wild-type mice. This is in agreement with backscattered electron (BSE) imaging results of the cross section of mice femoral mid-diaphysis (as also carried out in [15]), which showed 2D porosity coefficients of 1.68 ± 0.26 % and 29.57 ± 1.74 % for wild-type and GIOP bone, respectively.

Histograms of degree of mineralisation and the mean mineral concentration of middle shaft femoral bone from wild-type (N = 5) and GIOP (N = 5) mice were measured using X-ray microtomography. Representative distributions of mineral concentration were plotted for mid-shaft femora from wild-type and GIOP mice (Fig. 2E). While not clearly visible at the lower-magnification whole-bone CT slices in Fig. 2A–D, our prior work using backscattered electron microscopy on GIOP vs WT-femora (at similar age-points) showed that the mineralization of the endosteal region is clearly lower than the periosteal region in GIOP, while it is similar across regions in WT [33]. Since two distinct regions of interest: endosteal region surrounded by less mineralized halos, and periosteal region, were observed in GIOP mice (Fig. 2C, D)[33], they were used separately for quantitative X-ray microtomography analysis (Fig. 2 inset C1). The weighted average mineral concentrations (denoted as the degree of mineralisation) measured as hydroxyapatite g/cm^3 were calculated from the frequency distribution of mineral concentration and plotted for different groups (Fig. 2E and F). One-way ANOVA test indicated that the mean mineral concentration among three groups were significantly different. The weighted average mineral concentration in wild-type mice is significantly higher than that in GIOP periosteal ($p < 0.01$) and endosteal regions ($p < 0.001$), and it is also significantly higher ($p < 0.01$) in GIOP periosteal regions compared to GIOP endosteal regions (Fig. 2F). The broad distribution of mineral concentration with a fat tail toward low mineral concentration in GIOP endosteal region indicated a microscale heterogeneous mineralisation.

3.2. In situ tensile testing with synchrotron SAXD and WAXD

3.2.1. SAXD and WAXD patterns

Representative SAXD and WAXD patterns for femoral mid-shaft of wild-type mice aged 24 weeks are shown in Fig. 1E and G, and 1D intensity profiles of the third-order collagen reflection and (002) mineral reflections in mice femur mid-diaphysis are shown in Fig. 1F and H.

3.2.2. Effective fibril moduli

To compare the fibrillar-deformation in mice femur tested at different strain rates (Figs. 5B and 4 A, D), data for samples at each strain rate were combined and plotted (tissue stress vs. nanoscale fibrillar strain) in the elastic deformation region (Fig. 4A, D), and show differences in the slope (effective fibril modulus $E_f = d\sigma/d\varepsilon_f$). Average effective fibril moduli from each group of samples were plotted as a function of strain rate in Fig. 5B (pink bars). As strain rate increased from 0.0004 s^{-1} to 0.02 s^{-1}, we observe a significant increase in the effective fibril modulus increased from 13.6 ± 3.0 S.D. GPa to 65.6 ± 11.4 S.D. GPa ($p < 0.001$) in wild-type mice bone.

In contrast, the effective fibril modulus remains nearly constant in GIOP mice bone (blue bars). The effective fibril modulus in wild-type mice are significantly ($p < 0.001$) higher compared to GIOP mice at strain rates 0.01 and 0.02 s^{-1}, no significant differences in the effective fibril modulus between wild-type and GIOP mice was found at strain rate 0.0004 s^{-1} (Fig. 4 and Table 3). Note that for the data plotted in Fig. 5B–D, the parameters E_f, E_m and rate of fibrillar reorientation are calculated per-sample and averaged within each strain-rate group, whilst the lines in Fig. 4 are regressions through the pooled data points (tissue stress vs fibril strain, mineral strain or reorientation) from all samples at that strain-rate. This difference accounts for slight differences in the slopes between the Figures: for example, the averaged fibril moduli in GIOP is lowest at the highest strain rate (0.02 %.s^{-1}; Fig. 5B) while the slope of the regression line for GIOP-bone in the fibril moduli plot in Fig. 4D is lowest for the intermediate strain rate 0.01 %.s^{-1}.

3.2.3. Effective mineral moduli

In a parallel manner, considering the mineral crystallite deformation, tissue stress versus mineral strain were grouped and plotted for three different strain rates (Fig. 4B, E). Here, the effective mineral modulus ($E_m = d\sigma/d\varepsilon_m$) in wild-type mice bone increased with strain rate and the increase was significant ($p = 0.026$) as seen in Fig. 5C (dark blue bars). E_m increased from 44.2 ± 7.3 S.D. GPa to 97.5 ± 28.3 S.D. GPa as strain rate increased from 0.0004 s^{-1} to 0.02 s^{-1} in wild-type mice bone. In contrast, E_m remains nearly constant in GIOP mice bone (blue bars). The effective mineral modulus in WT mice were significantly higher compared to GIOP mice at all strain rates (Fig. 4 and Table 3).

3.2.4. Fibrillar reorientation

Considering the fibrillar orientation with respect to the direction of loading, the azimuthal intensity distributions of the first-order collagen reflection from mice femur were used to determine the degree of fibrillar orientation (FWHM) at unstrained state and the change of FWHM during tensile loading. Wild-type mice bone shows that 1) the FWHM consistently narrows with increasing strain, but 2) the percentage-change reduces dramatically as the strain rate increases (Fig. 4C). Averaged values of the rate of fibrillar reorientation were plotted as a function of strain rate in Fig. 5D, and showed a significant ($p = 0.018$) reduction. In wild-type mice bone, the rate of fibrillar reorientation (-40.8 ± 23.2 S.D. °.%$^{-1}$) at low strain rate (0.0004 s^{-1}) is significantly higher as compared to strain rates of 0.01 s^{-1} ($p = 0.034$) and 0.02 s^{-1} ($p = 0.025$).

In contrast, for GIOP bone there are no significant differences in reorientation rate with strain rates. The reorientation rate in GIOP mice bone at strain rate 0004 s^{-1} is significantly lower than that in wild-type bone, whereas no significant differences in reorientation rate was found between wild-type and GIOP mice bone at strain rate 0.01 s^{-1} and 0.02 s^{-1} (Fig. 4 and Table 3).

3.3. Model fitting to experimental E_f, E_m and reorientation

An initial fitting process for the two models allowed the Young's moduli corresponding to the three analyzed strain rate values and the volume fraction of the extrafibrillar matrix (Fig. 5A) to be calculated. Fig. 5A shows the variation of the modulus of extrafibrillar matrix. In the wild-type case the extrafibrillar matrix stiffens by over a factor of 100 – from 3.5 GPa at $\dot{\varepsilon} = 0.0004\,s^{-1}$ (low strain rate) to 370.0 GPa at $\dot{\varepsilon} = 0.02\,s^{-1}$ (high strain rate). In the GIOP case, instead, depending on the imposed *k*-factor and on the strain rate, values of the extrafibrillar Young's modulus can range between 52.1 and 163.8 GPa (Table 2).

Fig. 5B shows a comparison between the experimental and numerically computed effective fibril modulus E_f. For the wild model, the results show agreement within the experimental error bars, underestimation at medium and high strain rate values and overestimation at the low strain rate ($\dot{\varepsilon} = 0.02\,s^{-1}$). For the wild-type model a stiffening effect with an increasing strain rate – as seen in experiment – was also found at the mineral level (Fig. 5C). The effective mineral modulus, E_m, is overestimated at high and medium strain rates and slightly underestimate at low strain rate.

For the GIOP bone, both the effective fibrillar and mineral moduli confirm the constant trend found experimentally (Fig. 5B and C) and show agreement with experimental values (average experimental 13.6 GPa vs 13.9 GPa). Indeed, the average experimental value of the effective fibril modulus at the 3 strain rates is 13.6 GPa while the corresponding modelling value is 13.9 GPa. Corresponding values for the effective mineral modulus are respectively 22.8 GPa and 21.8 GPa.

Fig. 5D shows that for lamellar-level fibrillar reorientation – calculated via change of $\Delta FWHM$ normalised by the fibril strain – the wild-type model reproduces the trend to reduced reorientation with increased stress. For the GIOP model a reduction of the *k*-factor (**Equation S6**) lead to a reduction of fibrillar reorientation (Fig. 5D). Our parametric analysis shows that the reorientation calculated via FE simulations matches the experimental reorientation (modelling values within the experimental error bars) for 3 strain rates assuming

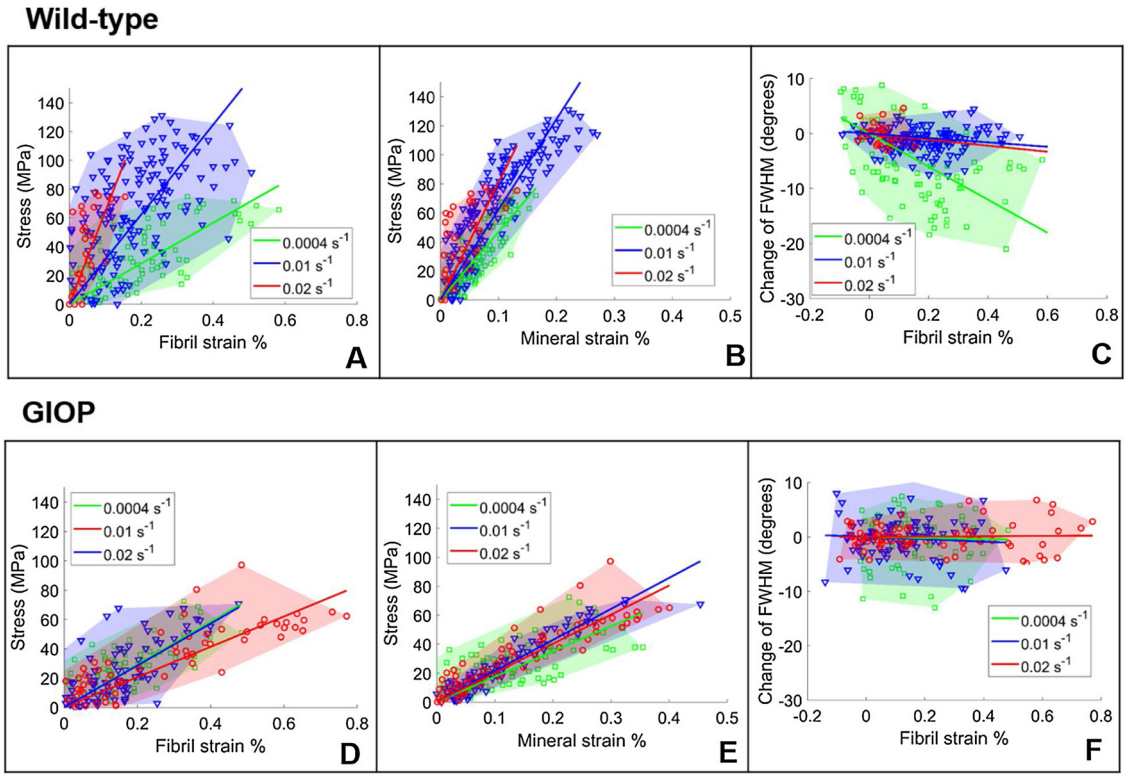

Fig. 4. Fibril strain, mineral strain and change of FWHM from in situ synchrotron SAXD and WAXD: Symbol code: Low strain rate (0.0004 s^{-1}, green squares), medium strain rate (0.01 s^{-1}, blue triangles) and high strain rate (0.02 s^{-1}, red circles). (A, D) Applied tissue stress vs average fibril strain. (B, E) Applied tissue stress vs average mineral strain. (C, F) Change of the FWHM of a Gaussian profile vs average fibril strain (see also text and Table 1 for parameter definitions). The symbols are experimental data points (pooled across samples for each strain rate) while the straight lines are linear regression lines for each group of data (regressions through pooled data points at a given strain-rate). The shadowed area in the six plots is a convex hull of the experimental data representing the region that numerical results are expected to intersect (for interpretation of the references to colour in this figure legend, the reader is referred to the web version of this article).

$k = 1.58$.

4. Discussion

Strain-rate dependent tensile tests were performed on small femoral samples of wild-type and steroid-induced osteoporotic (GIOP) mice. Our main findings can be summarized as follows:

- Under tensile testing with increasing strain rate, the fibrillar-level deformation of GIOP bone exhibits a contrasting behaviour to wild-type (WT; normal) murine bone – specifically, while WT-bone shows a significant increase in effective fibril- and mineral-moduli, this effect is absent in GIOP bone
- On increasing strain-rate, WT-bone shows a significant reduction of extent of fibrillar reorientation toward the loading axis; in contrast, GIOP bone shows no change in reorientation with strain-rate.
- By comparing the volume-average SAXS- and WAXD-measures of fibril- and mineral-strain to the model predictions of a fibril/fibril-array model of bone matrix mechanics, the strain-rate dependent effects in WT-bone are explained via an increased extrafibrillar matrix stiffening.
- In contrast, for GIOP-bone, the experimental results can be matched to model predictions if the reinforcement between mineral- and collagen (via the *k*-factor; Table 2) at the nanoscale is taken higher for GIOP compared to WT, and no extrafibrillar matrix stiffening occurs in GIOP-bone.

The novelty of the current study is primarily in obtaining experimental data characterising how the strain-rate dependence of fibrillar deformation mechanics in osteoporotic bone differ from normal cortical bone, and as a secondary goal, to explore the underlying structural mechanism by fitting a multilevel model to the data. Prior work, by our group as well as others [14,15,33,42] have analysed alterations in fibrillar mechanics in metabolic bone disorders like rickets, GIOP, and ageing, but these have not studied strain-rate dependence in such pathological conditions. Because bone is used in a dynamic mechanical environment, understanding how the structural response of the bone matrix at the fibrillar level alters with increasing strain rate is of direct interest. From a materials-standpoint, for example, our observation that the fibril strain gradient (from E_f) is unchanged at different strain rates in GIOP-bone, but decreases in WT-bone (Fig. 4), provides insight into the altered biomechanical reinforcing efficiency of the collagen fibrils. Further, while the current work does not directly deal with fracture, prior work by other groups has shown that strain-rate influences work of fracture, with reduction of work of fracture and transition to unstable crack growth with increasing strain rate [62,63], as well as increase of elastic moduli and yield strength [64]. Indeed, if fibrils in osteoporotic GIOP bone show no change with increasing strain rate, while an effective "stiffening" is seen via the increased fibril modulus in normal (WT) bone, this may lead to a lower mechanical competence in GIOP at higher strain-rates compared to WT. When compared with the wild-type bone, the relationship between strain rate and increasing modulus breaks down for GIOP, indicating the mineral-collagen composite in GIOP failed to adequately stiffen with increasing strain rate, which is likely the cause of the lowered mechanical competence. While the lower maximal fibril strain in WT relative to GIOP sounds counter-intuitive when one associates disease with lowered strength and brittleness, we note that a) the total tissue strain is a complex sum of the fibril, interfibrillar, and interlamellar level strains and b) the maximal elastic stress level in GIOP is lower than WT. Therefore, the expected

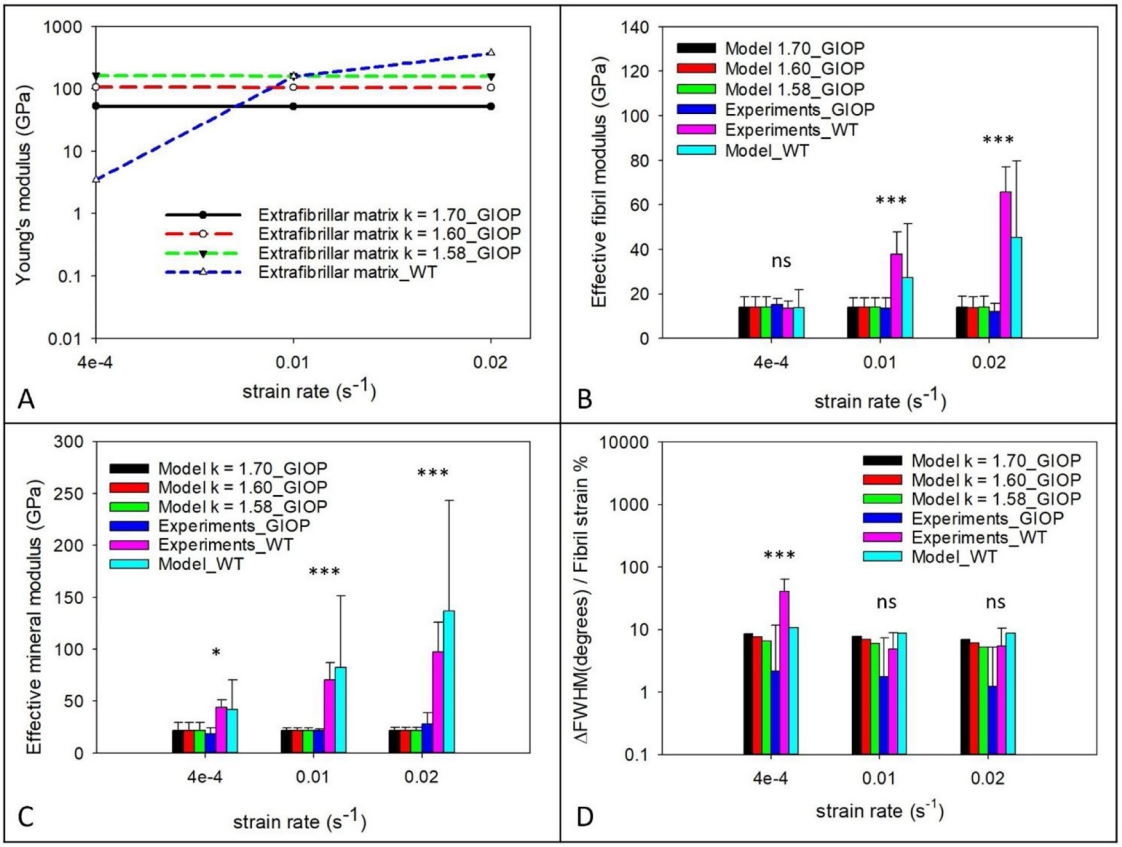

Fig. 5. Nanoscale structural parameters of bone mineral and fibrils from experiments and modelling: (A) Young's modulus of collagen and extrafibrillar matrix at different strain rates from simulation results (in log scale). (B) Effective fibril modulus, (C) effective mineral modulus and (D) reorientation rate (in log scale) are plotted as a function of strain-rate. Error bars shown are standard deviations for experimental data while are 95 % confidence interval from the fitting process. One-way ANOVA tests were performed to test for statistical differences in the experimental results of the effective fibril modulus, the effective mineral modulus and the fibrillar reorientation rate between samples tested at different strain-rates. Statistical significance is denoted (*p < 0.05, **p < 0.01, ***p < 0.001, ns: not significant).

Table 3
Effective fibril moduli, effective mineral moduli and fibrillar reorientation in WT- and GIOP-bone; p-values report differences between WT- and GIOP- in each group.

	Strain rate (s^{-1})	Wild-type	GIOP	*p*-value
Effective fibril moduli (GPa)	0.004	13.60 ± 3.00	14.46 ± 2.66	0.876
	0.01	37.90 ± 9.90	13.02 ± 4.28	< 0.001
	0.02	65.60 ± 11.40	11.50 ± 3.58	< 0.001
Effective mineral moduli (GPa)	0.004	44.20 ± 7.29	17.90 ± 5.30	0.032
	0.01	70.50 ± 16.70	20.77 ± 1.42	< 0.001
	0.02	97.49 ± 28.38	26.66 ± 10.50	< 0.001
Reorientation rate (degree/%)	0.004	40.75 ± 23.22	2.18 ± 9.65	< 0.001
	0.01	4.90 ± 3.91	1.76 ± 5.63	0.703
	0.02	5.50 ± 4.94	1.24 ± 4.02	0.606

weak (lower strength) behavior in GIOP is present, whilst the lower maximal fibril strain in WT- does not exclude that the maximal strain at macroscopic failure will still be lower in GIOP than WT (possibly due to tissue-level defects and pores). We note, however, an underlying assumption in our work is that the mouse model of endogenous glucocorticoid production (Cushing's syndrome) is a valid and relevant model for (exogenous) human GIOP [40]. As mouse models do not exhibit secondary remodelling, the bone structure at the tissue level will be different from human GIOP.

The strain-rate dependence of the mechanical properties of bone have been studied at the macroscopic level before [58,64–66], using phenomenological viscoelastic/viscoplastic models or relations such as the Ramberg-Osgood equation used earlier. The nature of the structural mechanisms in time-dependent mechanical loading is less studied. High strain-rate *in situ* SAXD measurements on human bone found a strain-rate induced stiffening of the fibril ductility associated with a loss in toughness in bone matrix [38], and compressive creep studies found the strain on both mineral and collagen phases in bone increase linearly with time, proposed as a load-shedding from collagen to mineral [67]. Stress-relaxation was observed to be more rapid in mineral than in collagen [68]. Molecular dynamics studies (e.g [69].) have highlighted the role of rapidly breaking and reforming hydrogen bonds during deformation. Nevertheless, structural-mechanisms enabling viscoelasticity in the bone matrix are not clearly known, and the experimental data on the variation of the time-dependent behaviour in osteoporosis presented here may help toward that eventual goal. It is noted that the exposure of the samples to X-rays is consistent across three different strain-rates. By closing the shutter between acquisitions, and keeping acquisition time constant at 0.1 s per point, the total X-ray dose is proportional to the number of SAXS patterns per tensile test. Fig. S5 (Supplementary Information) shows that the number of patterns is of the same order of magnitude across strain-rates. Therefore, it is not likely that the high-strain rate tests are being exposed to much higher X-ray dosages compared to the low- and medium strain-rates, which would cause damage to the collagen matrix [44].

The experimental values for maximal fibril strain (Fig. 5A) at low strain rates (~0.4-0.6 %) are consistent with our prior quasi-static results on both murine [15,33,42] and bovine bone [37], and in the same range as those observed by others on human bone [14]. In WT-bone, the maximal fibril strain reduces consistently from ~0.6 % at the lowest

strain rate (0.0004 s^{-1}) to ~0.1 % at the highest strain-rates (0.02 s^{-1}). However, a similar trend is not visible for GIOP; for intermediate strain rates (0.01 s^{-1}) in GIOP-osteoporotic bone – in Fig. 4D, maximum fibril strain can reach ~0.6-0.8 % compared to the ~0.4 % values for the lowest strain-rate, while for the highest strain rate the maximum fibril strain is again ~0.4 %. Since maximum strains are linked to strength and failure of the entire bone, microstructural differences between GIOP- and wild-type bone (Fig. 2) may be relevant in explaining this behaviour, which is beyond the scope of the nano/microscale model presented and discussed below.

Fibrillar reorientation, as well, shows some notable differences between GIOP and WT. Here, it is important to note certain experimental limitations. As SAXD and WAXD provide volume averaged measures of fibrillar/mineral structure through the thickness of cortical bone specimens used in these tests, effects *below* and *above* the scale of the fibril cannot be excluded. Consequently, if the sample volume contained microscopically misaligned lamellae, these could undergo inter-lamellar reorientation, rather than the reorientation occurring at the fibril/interfibrillar matrix alone (this corresponds to phenomena above the scale of the fibril). Likewise, it is known that tropocollagen molecules inside microfibrils are arranged in a tilted geometry [70] and intrafibrillar rearrangement may also contribute, rather than fibrils rotating in a rigid-body manner. However, we note that the numerical value of the tilt inside microfibrils is small (~4° in Figs. 2 and 3 in [70]) (noting the factor of 5 compression in the c-axis direction specified by the authors). This value is much smaller (Fig. 5D) compared to the ~50° (FWHM change)/% strain reorientation seen for the lowest strain rate. Therefore, load-induced intrafibrillar rotation of the molecules, to remove the tilt, would be insufficient to explain the magnitude of the observed reduction in FWHM. To be able to overcome the averaging issue inherent in our experimental configuration, possible future routes may involve 6D SAXS tensor tomography [71], if challenges in data processing and potential radiation damage are overcome. Such methods can provide spatially-resolved 3D maps of the fibrillar nanostructure across the tissue, although time-resolved studies at the strain-rates proposed here (and above) will still be challenging. Subfibrillar-level deformation may be analysed by the covariation of changes in the angular intensities of the WAXD and SAXS patterns (which will provide information on how the mineral particles are reorienting relative to the fibrils), or possibly by contrast-variation neutron diffraction to resolve the changes in tropocollagen ordering.

While the empirical differences between the strain-rate dependencies in the GIOP- and WT-nanoscale parameters (E_f and E_m) is clear from Figs. 4, 5, these numbers (averaged across scattering volume) by themselves do not provide a full structural explanation. From our earlier studies on GIOP-bone [15,33], the orientation distribution is wider in GIOP that WT. These facts imply that earlier simpler models, such as our prior work on antler [36], which modelled the uniaxial fibrils alone (oriented along the loading axis), are likely insufficient to explain the data. As a first step in this direction, we used a two-level multiscale model of bone nano- and microstructure to provide some insights into possible reasons for these changes. At the fibrillar level, the model is similar to prior staggered models of mineral-collagen interactions put forward [11,36,41,55–57,61,72], although the inclusion of the mechanics of the extrafibrillar matrix is an advance on our prior modelling [36]. At the fibril-array level (microscale), bone is known to have a lamellar structure although the precise details of the orientation (originally proposed as plywood or rotated plywood [13,73]) are still not fully clear, with recent revisions to the orientation scheme proposed [12] to incorporate a fraction (10 %) of disordered fibrils. The plywood scheme used in the original paper [13] is used here (also for consistency with prior modelling work [61]), but inclusion of more complex structures to model the experimental results is possible in the future. Further, the microstructure of rat and mice bone is different from human bone, which has extensive secondary remodelling and well developed secondary osteons, and these differences are not accounted for in the model. In addition, spatial variations in bone matrix parameters at larger length scales than the nano- and micro- (such as across cross-sections of cortical bone reported in rat bone [74]) are beyond the scope of the model, even though clear variations between endosteal and periosteal regions (Fig. 2) are visible. Parameter estimates from the model and their structural interpretation below need therefore to be considered as estimates rather than definitive values.

From optimizing the parameters for model predictions to agree with experimental values of effective fibril- and mineral-moduli, it is observed that in normal WT cortical bone the stiffening of the extrafibrillar matrix with increasing strain-rate can lead to the increased fibril (and mineral) modulus seen experimentally (Fig. 5). Increased stress borne by the extrafibrillar matrix reduces the strain on the fibrils, which therefore increases the effective fibril modulus, which is a ratio of macroscopic stress to fibril strain. A similar process occurs for effective mineral moduli. The extrafibrillar space in bone contains extrafibrillar mineral and non-collagenous proteins [75,76], and we can speculate that such a phase of mineral interlinked with protein may exhibit strain-stiffening behaviour with increasing strain-rate, being dominated by the moduli of the noncollageneous proteins (< 1 GPa) at low strain rates and by the modulus of the mineral at larger strain rates. However, we obtain unrealistically high values for the modulus of the extrafibrillar matrix (370 GPa) at the highest strain rate, well above the 100 − 110 GPa characteristic of hydroxyapatite mineral [36]. Possibly, these values arise from the extrafibrillar volume fraction or type of orientation distribution used here, and parametric-variation studies may be useful in future in this regard.

In contrast, the experimental data for the GIOP-bone can be fit to the model with essentially constant extrafibrillar matrix moduli (Table 2) but with a considerably lowered *k*-factor. The physical meaning of this difference compared to WT bone is not fully clear. The *k*-factor is inversely linked to the reinforcing efficiency of the mineral platelets inside the collagen fibril [11,36], and arises due to the load-transfer from the collagen matrix to the mineral platelet. Note that the effect of the more random fibril orientation in GIOP [15,33] has already been included via the wider FWHM from $I(\chi)$. As the *k*-factor depends on the effectiveness with which loads are transferred to the mineral from the collagen, the differing *k*-factor in GIOP compared to WT suggests that possibly the orientation and/or interactions of intrafibrillar mineral with collagen may differ. However, this still does not explain why we do not obtain a similar strain-rate dependent stiffening as seen in WT-bone. We can speculate that these open questions are linked to limitations of our model. As the fibril orientation distribution is not precisely the multilayer lamellar structure described initially [13] but includes random fibril orientations [12], and the further differences in lamellar structure in GIOP have not yet been determined, it is likely that further alterations or refinements to the structural model will be needed, even though the experimental differences between GIOP- and WT-bone fibrillar strain-rate dependencies are not in question.

A limitation of the current work is that we did not report results of varying the collagen- and mineral-moduli in the model, both of which may change in disease due to substitution of ions and change in covalent crosslinking [14,77]. In this regard, we have observed (data not shown) that variation of collagen moduli cannot explain the increase in effective mineral moduli (Fig. 5C) with strain rate. Regarding the mineral phase, our previous study [15] showed that, compared to WT bone, the mineral platelet is slightly shorter (in length, along the c-axis) and the intra-platelet lattice spacing is slightly higher in GIOP bone, but the mechanical implications of these crystallographic changes is not clear to us at this point. Perhaps, future *ab initio* molecular dynamics simulations of the change in mineral crystallite structure [78], linked to simulated mechanical testing at these small scales, could shed light on this question.

In summary, we have analysed for the first time the fibrillar- and mineral-level strain changes in steroid-induced osteoporotic and

normal murine bone with increasing strain-rate, and have found both a) clear changes with strain-rate for normal bone and b) a near constant-response across strain-rates for osteoporotic bone. Modelling the bone matrix as arrays of mineralized fibrils with intervening matrix, our results suggest alterations in extrafibrillar matrix stiffness and mineral-collagen reinforcement factors may be the underlying factors. Our results provide insight into the time-dependent nature of fibrillar mechanics in both normal and osteoporotic bone, and may be relevant in understanding the structural origins (in terms of bone quality) of the lower mechanical competence in osteoporosis.

Acknowledgments

This work was supported by Diamond Light Source (Harwell, UK), Queen Mary University of London (grant no. SEML1B4R), the Medical Research Council UK (grant no. G0600702) and the National Science and Technology Major Project (2017-VI-0020-0093). L.X. is supported by the China Scholarship Council (CSC) and the China Postdoctoral Science Foundation. NMP is supported by the European Commission with the Graphene Flagship Core 2 n. 785219 (WP14 “Composites”) and FET Proactive “Neurofibres” n. 732344 as well as by the MIUR with the “Departments of Excellence” grant L. 232/2016, ARS01-01384-PROSCAN Grant and the PRIN-20177TTP3S. We thank Diamond Light Source (Harwell, UK) for the award of synchrotron beamtime to carry out the *in situ* SAXD/WAXD experiments (SM9893, SM11806, and SM12483). HSG acknowledges support from BBSRC (BB/R003610/1) and from UKRI (MR/R025673/1). NJT acknowledges support from BBSRC (BB/R004773/1)

Appendix A. Supplementary data

Supplementary material related to this article can be found, in the online version, at doi:https://doi.org/10.1016/j.bone.2019.115111.

References

[1] J.A. Kanis, Diagnosis of osteoporosis and assessment of fracture risk, Lancet 359 (9321) (2002) 1929–1936.
[2] E. Seeman, P.D. Delmas, Bone quality–the material and structural basis of bone strength and fragility, N. Engl. J. Med. 354 (21) (2006) 2250–2261.
[3] A. Carriero, E.A. Zimmermann, A. Paluszny, S.Y. Tang, H. Bale, B. Busse, T. Alliston, G. Kazakia, R.O. Ritchie, S.J. Shefelbine, How tough is brittle bone? Investigating osteogenesis imperfecta in mouse bone, J. Bone Miner. Res. 29 (6) (2014) 1392–1401.
[4] J.D. Currey, The structure and mechanics of bone, J. Mater. Sci. 47 (1) (2012) 41–54.
[5] J. Currey, Bones: Structure and Mechanics, Princeton University Press, 2002.
[6] J.D. Currey, Mechanical properties of vertebrate hard tissues, Proc. Inst. Mech. Eng. H 212 (H6) (1998) 399–411.
[7] J.D. Currey, Effects of strain rate, reconstruction and mineral content on some mechanical-properties of bovine bone, J. Biomech. 8 (1) (1975) 81–86.
[8] J.D. Currey, Role of collagen and other organics in the mechanical properties of bone, Osteoporos. Int. 14 (2003) S29–S36.
[9] P. Zioupos, J.D. Currey, A.J. Hamer, The role of collagen in the declining mechanical properties of aging human cortical bone, J. Biomed. Mater. Res. 45 (2) (1999) 108–116.
[10] S. Weiner, H.D. Wagner, The material bone: structure mechanical function relations, Ann. Rev. Mater. Sci. 28 (1998) 271–298.
[11] P. Fratzl, R. Weinkamer, Nature’s hierarchical materials, Prog. Mater. Sci. 52 (8) (2007) 1263–1334.
[12] N. Reznikov, R. Shahar, S. Weiner, Bone hierarchical structure in three dimensions, Acta Biomater. 10 (9) (2014) 3815–3826.
[13] S. Weiner, W. Traub, H.D. Wagner, Lamellar bone: structure–function relations, J. Struct. Biol. 126 (3) (1999) 241–255.
[14] E.A. Zimmermann, E. Schaible, H. Bale, H.D. Barth, S.Y. Tang, P. Reichert, B. Busse, T. Alliston, J.W. Ager, R.O. Ritchie, Age-related changes in the plasticity and toughness of human cortical bone at multiple length scales, Proc. Natl. Acad. Sci. 108 (35) (2011) 14416–14421.
[15] L. Xi, P. De Falco, E. Barbieri, A. Karunaratne, L. Bentley, C.T. Esapa, N.J. Terrill, S.D.M. Brown, R.D. Cox, G.R. Davis, N.M. Pugno, R.V. Thakker, H.S. Gupta, Bone matrix development in steroid-induced osteoporosis is associated with a consistently reduced fibrillar stiffness linked to altered bone mineral quality, Acta Biomater. 76 (2018) 295–307.
[16] P.J. Thurner, C.G. Chen, S. Ionova-Martin, L. Sun, A. Harman, A. Porter, J.W. Ager 3rd, R.O. Ritchie, T. Alliston, Osteopontin deficiency increases bone fragility but preserves bone mass, Bone 46 (6) (2010) 1564–1573.
[17] T.P. Van Staa, R.F. Laan, I.P. Barton, S. Cohen, D.M. Reid, C. Cooper, Bone density threshold and other predictors of vertebral fracture in patients receiving oral glucocorticoid therapy, Arthritis Rheum. 48 (11) (2003) 3224–3229.
[18] J. Compston, Management of glucocorticoid-induced osteoporosis, Nat. Rev. Rheumatol. 6 (2) (2010) 82–88.
[19] F. Mirza, E. Canalis, Secondary osteoporosis: pathophysiology and management, Eur. J. Endocrinol. 173 (3) (2015) R131–R151.
[20] R. Rizzoli, E. Biver, Glucocorticoid-induced osteoporosis: who to treat with what agent? Nat. Rev. Rheumatol. 11 (2) (2015) 98–109.
[21] A.L. Boskey, E. DiCarlo, E. Paschalis, P. West, R. Mendelsohn, Comparison of mineral quality and quantity in iliac crest biopsies from high- and low-turnover osteoporosis: an FT-IR microspectroscopic investigation, Osteoporos. Int. 16 (12) (2005) 2031–2038.
[22] W.J. Landis, An overview of vertebrate mineralization with emphasis on collagen-mineral interaction, Gravit. Space Biol. Bull. 12 (2) (1999) 15–26.
[23] E. Canalis, G. Mazziotti, A. Giustina, J.P. Bilezikian, Glucocorticoid-induced osteoporosis: pathophysiology and therapy, Osteoporos. Int. 18 (10) (2007) 1319–1328.
[24] R.C. Pereira, A.M. Delany, E. Canalis, Effects of cortisol and bone morphogenetic protein-2 on stromal cell differentiation: correlation with CCAAT-enhancer binding protein expression, Bone 30 (5) (2002) 685–691.
[25] V. Krishnan, H.U. Bryant, O.A. MacDougald, Regulation of bone mass by Wnt signaling, J. Clin. Invest. 116 (5) (2006) 1202–1209.
[26] E. Canalis, Wnt signalling in osteoporosis: mechanisms and novel therapeutic approaches, nature reviews, Endocrinology 9 (10) (2013) 575–583.
[27] D. Jia, C.A. O’Brien, S.A. Stewart, S.C. Manolagas, R.S. Weinstein, Glucocorticoids act directly on osteoclasts to increase their life span and reduce bone density, Endocrinology 147 (12) (2006) 5592–5599.
[28] H.J. Kim, H.B. Zhao, H. Kitaura, S. Bhattacharyya, J.A. Brewer, L.J. Muglia, F.P. Ross, S.L. Teitelbaum, Glucocorticoids suppress bone formation via the osteoclast, J. Clin. Invest. 116 (8) (2006) 2152–2160.
[29] P. Orcel, Updated recommendations on the management of glucocorticoid-induced osteoporosis, Joint Bone Spine 81 (6) (2014) 465–468.
[30] K. Hayashi, M. Yamamoto, Y. Murakawa, M. Yamauchi, H. Kaji, T. Yamaguchi, T. Sugimoto, Bone fragility in male glucocorticoid-induced osteoporosis is not defined by bone mineral density, Osteoporos. Int. 20 (11) (2009) 1889–1894.
[31] N.E. Lane, W. Yao, M. Balooch, R.K. Nalla, G. Balooch, S. Habelitz, J.H. Kinney, L.F. Bonewald, Glucocorticoid-treated mice have localized changes in trabecular bone material properties and osteocyte lacunar size that are not observed in placebo-treated or estrogen-deficient mice, J. Bone Miner. Res. 21 (3) (2006) 466–476.
[32] R.S. Weinstein, D. Jia, C.C. Powers, S.A. Stewart, R.L. Jilka, A.M. Parfitt, S.C. Manolagas, The skeletal effects of glucocorticoid excess override those of orchidectomy in mice, Endocrinology 145 (4) (2004) 1980–1987.
[33] A. Karunaratne, L. Xi, L. Bentley, D. Sykes, A. Boyde, C.T. Esapa, N.J. Terrill, S.D.M. Brown, R.D. Cox, R.V. Thakker, H.S. Gupta, Multiscale alterations in bone matrix quality increased fragility in steroid induced osteoporosis, Bone 84 (2016) 15–24.
[34] S.L. Greenspan, A. Wyman, F.H. Hooven, S. Adami, S. Gehlbach, F.A. Anderson Jr., S. Boone, A.Z. Lacroix, R. Lindsay, J. Coen Netelenbos, Predictors of treatment with osteoporosis medications after recent fragility fractures in a multinational cohort of postmenopausal women, J. Am. Geriatr. Soc. 60 (3) (2012) 455–461.
[35] V. Elliot-Gibson, E. Bogoch, S. Jamal, D. Beaton, Practice patterns in the diagnosis and treatment of osteoporosis after a fragility fracture: a systematic review, Osteoporos. Int. 15 (10) (2004) 767–778.
[36] H. Gupta, S. Krauss, M. Kerschnitzki, A. Karunaratne, J. Dunlop, A. Barber, P. Boesecke, S. Funari, P. Fratzl, Intrafibrillar plasticity through mineral/collagen sliding is the dominant mechanism for the extreme toughness of antler bone, J. Mech. Behav. Biomed. Mater. 28 (2013) 366–382.
[37] H.S. Gupta, J. Seto, W. Wagermaier, P. Zaslansky, P. Boesecke, P. Fratzl, Cooperative deformation of mineral and collagen in bone at the nanoscale, Proc. Natl. Acad. Sci. U. S. A. 103 (47) (2006) 17741–17746.
[38] E.A. Zimmermann, B. Gludovatz, E. Schaible, B. Busse, R.O. Ritchie, Fracture resistance of human cortical bone across multiple length-scales at physiological strain rates, Biomaterials 35 (21) (2014) 5472–5481.
[39] L. Bentley, C.T. Esapa, M.A. Nesbit, R.A. Head, H. Evans, D. Lath, C.L. Scudamore, T.A. Hough, C. Podrini, F.M. Hannan, W.D. Fraser, P.I. Croucher, M.A. Brown, S.D.M. Brown, R.D. Cox, R.V. Thakker, An N-ethyl-n-nitrosourea induced corticotropin-releasing hormone promoter mutation provides a mouse model for endogenous glucocorticoid excess, Endocrinology 155 (3) (2014) 908–922.
[40] M. Toth, A. Grossman, Glucocorticoid-induced osteoporosis: lessons from Cushing’s syndrome, Clin. Endocrinol. 79 (1) (2013) 1–11.
[41] I. Jager, P. Fratzl, Mineralized collagen fibrils: a mechanical model with a staggered arrangement of mineral particles, Biophys. J. 79 (4) (2000) 1737–1746.
[42] A. Karunaratne, C.R. Esapa, J. Hiller, A. Boyde, R. Head, J.H. Bassett, N.J. Terrill, G.R. Williams, M.A. Brown, P.I. Croucher, S.D. Brown, R.D. Cox, A.H. Barber, R.V. Thakker, H.S. Gupta, Significant deterioration in nanomechanical quality occurs through incomplete extrafibrillar mineralization in rachitic bone: evidence from in-situ synchrotron X-ray scattering and backscattered electron imaging, J. Bone Miner. Res. 27 (4) (2012) 876–890.
[43] A. Karunaratne, A. Boyde, C.T. Esapa, J. Hiller, N.J. Terrill, S.D. Brown, R.D. Cox, R.V. Thakker, H.S. Gupta, Symmetrically reduced stiffness and increased extensibility in compression and tension at the mineralized fibrillar level in rachitic bone, Bone (2012).
[44] H.D. Barth, M.E. Launey, A.A. Macdowell, J.W. Ager 3rd, R.O. Ritchie, On the effect of X-ray irradiation on the deformation and fracture behavior of human cortical

bone, Bone 46 (6) (2010) 1475–1485.
[45] H.S. Gupta, J. Seto, W. Wagermaier, P. Zaslansky, P. Boesecke, P. Fratzl, Cooperative deformation of mineral and collagen in bone at the nanoscale, Proc. Natl. Acad. Sci. U. S. A. 103 (47) (2006) 17741–17746.
[46] H.S. Gupta, W. Wagermaier, G.A. Zickler, D. Raz-Ben Aroush, S.S. Funari, P. Roschger, H.D. Wagner, P. Fratzl, Nanoscale deformation mechanisms in bone, Nano Lett. 5 (10) (2005) 2108–2111.
[47] W.J. Landis, K.J. Hodgens, J. Arena, M.J. Song, B.F. McEwen, Structural relations between collagen and mineral in bone as determined by high voltage electron microscopic tomography, Microsc. Res. Tech. 33 (2) (1996) 192–202.
[48] M. Basham, J. Filik, M.T. Wharmby, P.C. Chang, B. El Kassaby, M. Gerring, J. Aishima, K. Levik, B.C. Pulford, I. Sikharulidze, Data analysis WorkbeNch (DAWN), J. Synchrotron Radiat. 22 (3) (2015) 853–858.
[49] A. Karunaratne, C.R. Esapa, J. Hiller, A. Boyde, R. Head, J.H. Bassett, N.J. Terrill, G.R. Williams, M.A. Brown, P.I. Croucher, S.D. Brown, R.D. Cox, A.H. Barber, R.V. Thakker, H.S. Gupta, Significant deterioration in nanomechanical quality occurs through incomplete extrafibrillar mineralization in rachitic bone: evidence from in-situ synchrotron X-ray scattering and backscattered electron imaging, J. Bone Miner. Res. 27 (4) (2012) 876–890.
[50] M.J. Berger, J.H. Hubbell, S.M. Seltzer, J. Chang, J.S. Coursey, R. Sukumar, D.S. Zucker, K. Olsen, XCOM: Photon Cross Section Database, (2010).
[51] I. Zizak, P. Roschger, O. Paris, B.M. Misof, A. Berzlanovich, S. Bernstorff, H. Amenitsch, K. Klaushofer, P. Fratzl, Characteristics of mineral particles in the human bone/cartilage interface, J. Struct. Biol. 141 (3) (2003) 208–217.
[52] H.S. Gupta, S. Schratter, W. Tesch, P. Roschger, A. Berzlanovich, T. Schoeberl, K. Klaushofer, P. Fratzl, Two different correlations between nanoindentation modulus and mineral content in the bone-cartilage interface, J. Struct. Biol. 149 (2) (2005) 138–148.
[53] D. Planchard, SOLIDWORKS 2017 Reference Guide, SDC Publications, 2017.
[54] Hibbett, Karlsson, Sorensen, ABAQUS/standard: User's Manual, Hibbitt, Karlsson & Sorensen, 1998.
[55] H.J. Gao, B.H. Ji, I.L. Jager, E. Arzt, P. Fratzl, Materials become insensitive to flaws at nanoscale: lessons from nature, Proc. Natl. Acad. Sci. U. S. A. 100 (10) (2003) 5597–5600.
[56] B. Ji, H. Gao, Elastic properties of nanocomposite structure of bone, Compos. Sci. Technol. 66 (9) (2006) 1209–1215.
[57] B. Bar-On, H.D. Wagner, Mechanical model for staggered bio-structure, J. Mech. Phys. Solids 59 (9) (2011) 1685–1701.
[58] T.K. Hight, J.F. Brandeau, Mathematical-modeling of the stress-strain strain rate behavior of bone using the ramberg-osgood equation, J. Biomech. 16 (6) (1983) 445–450.
[59] W. Yang, V.R. Sherman, B. Gludovatz, E. Schaible, P. Stewart, R.O. Ritchie, M.A. Meyers, On the tear resistance of skin, Nat. Commun. 6 (2015) 6649.
[60] W.H. Press, S.A. Teukolsky, W.T. Vetterling, B.P. Flannery, Numerical Recipes 3rd Edition: The Art of Scientific Computing, Cambridge University Press, 2007.
[61] A. Vercher, E. Giner, C. Arango, J.E. Tarancón, F.J. Fuenmayor, Homogenized stiffness matrices for mineralized collagen fibrils and lamellar bone using unit cell finite element models, Biomech. Modell. Mechanobiol. 13 (2) (2014) 437–449.
[62] A. Ural, P. Zioupos, D. Buchanan, D. Vashishth, The effect of strain rate on fracture toughness of human cortical bone: a finite element study, J. Mech. Behav. Biomed. Mater. 4 (7) (2011) 1021–1032.
[63] S. Charoenphan, A. Polchai, Finite element modeling for strain rate dependency of fracture resistance in compact bone, J. Biomech. Eng. 129 (1) (2007) 20–25.
[64] U. Hansen, P. Zioupos, R. Simpson, J.D. Currey, D. Hynd, The effect of strain rate on the mechanical properties of human cortical bone, J. Biomech. Eng. 130 (1) (2008) 011011.
[65] Z. Asgharpour, P. Zioupos, M. Graw, S. Peldschus, Development of a strain rate dependent material model of human cortical bone for computer-aided reconstruction of injury mechanisms, Forensic Sci. Int. 236 (2014) 109–116.
[66] T.P.M. Johnson, S. Socrate, M.C. Boyce, A viscoelastic, viscoplastic model of cortical bone valid at low and high strain rates, Acta Biomater. 6 (10) (2010) 4073–4080.
[67] A.C. Deymier-Black, F. Yuan, A. Singhal, J.D. Almer, L.C. Brinson, D.C. Dunand, Evolution of load transfer between hydroxyapatite and collagen during creep deformation of bone, Acta Biomater. 8 (1) (2012) 253–261.
[68] J. Akbarzadeh, S. Puchegger, A. Stojanovic, H.O.K. Kirchner, W.H. Binder, S. Bernstorff, P. Zioupos, H. Peterlik, Timescales of self-healing in human bone tissue and polymeric ionic liquids, Bioinspir. Biom. Nanobiomater. 3 (3) (2014) 123–130.
[69] D. Lau, O. Büyüköztürk, M.J. Buehler, Multiscale modeling of organic-inorganic interface: from molecular dynamics simulation to finite element modeling, Mater. Res. Soc. Symp. Proc. (2012) 44–49.
[70] J.P.R.O. Orgel, T.C. Irving, A. Miller, T.J. Wess, Microfibrillar structure of type I collagen in situ, Proc. Natl. Acad. Sci. 103 (24) (2006) 9001.
[71] M. Liebi, M. Georgiadis, A. Menzel, P. Schneider, J. Kohlbrecher, O. Bunk, M. Guizar-Sicairos, Nanostructure surveys of macroscopic specimens by small-angle scattering tensor tomography, Nature 527 (7578) (2015) 349.
[72] M. Qwamizadeh, Z. Zhang, K. Zhou, Y.W. Zhang, On the relationship between the dynamic behavior and nanoscale staggered structure of the bone, J. Mech. Phys. Solids 78 (2015) 17–31.
[73] M.-M. Giraud-Guille, Plywood structures in nature, Curr. Opin. Solid State Mater. Sci. 3 (3) (1998) 221–227.
[74] M.J. Turunen, J.D. Kaspersen, U. Olsson, M. Guizar-Sicairos, M. Bech, F. Schaff, M. Tägil, J.S. Jurvelin, H. Isaksson, Bone mineral crystal size and organization vary across mature rat bone cortex, J. Struct. Biol. 195 (3) (2016) 337–344.
[75] A.A. Poundarik, T. Diab, G.E. Sroga, A. Ural, A.L. Boskey, C.M. Gundberg, D. Vashishth, Dilatational band formation in bone, Proc. Natl. Acad. Sci. U. S. A. 109 (47) (2012) 19178–19183.
[76] T. Hassenkam, G.E. Fantner, J.A. Cutroni, J.C. Weaver, D.E. Morse, P.K. Hansma, High-resolution AFM imaging of intact and fractured trabecular bone, Bone 35 (1) (2004) 4–10.
[77] Y. Wang, S. Von Euw, G. Laurent, C. Crevant, L. Bonhomme-Coury, M.M. Giraud-Guille, F. Babonneau, N. Nassif, T. Azais, Impact of collagen confinement vs. Ionic substitutions on the local disorder in bone and biomimetic apatites, Mater Horizons 1 (2) (2014) 224–231.
[78] W.Y. Ching, P. Rulis, A. Misra, Ab initio elastic properties and tensile strength of crystalline hydroxyapatite, Acta Biomater. 5 (8) (2009) 3067–3075.
[79] Y. Bouligand, Twisted fibrous arrangements in biological materials and cholesteric mesophases, Tissue Cell 4 (2) (1972) 189–217.

Supplementary Information:

Figure S1: Typical SAXD patterns of mice femur at different stress levels.

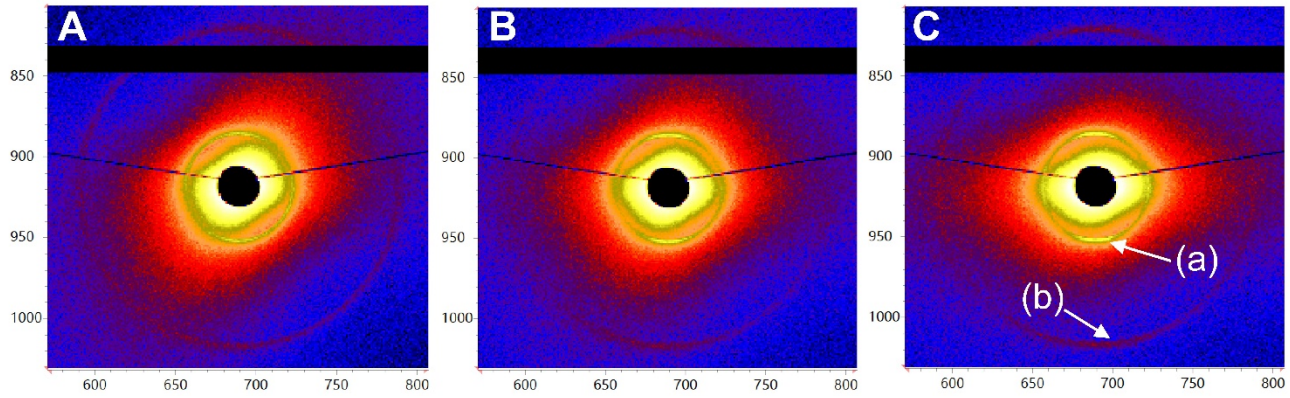

Figure S1: SAXD patterns of mice femoral mid-shaft at different stress levels σ. *(A) σ = 0 MPa, (B) σ = 36.8 MPa, and (C) σ = 74.5 MPa. The first-order (a) and the third-order (b) collagen reflection were indicated in (C).*

Figure S2: Azimuthal intensity profile of the first-order collagen peak of mice femoral mid-shaft at different stress levels.

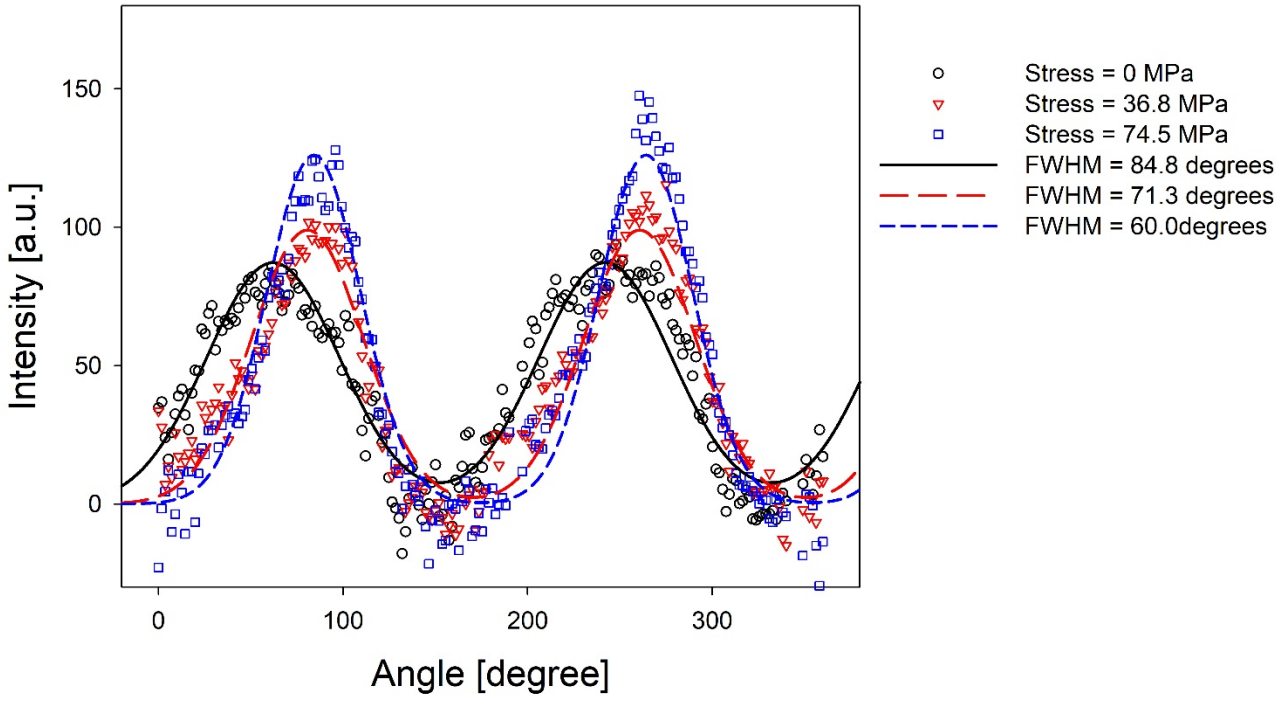

Figure S2: *The corrected azimuthal intensity profile (angle: azimuthal angle on the 2D SAXS detector plane,* ***Figure 1E****) of the first-order collagen peak from SAXD patterns of femoral mid-shaft at different stress levels.*

Figure S3-4： The intercepts of linear regressions of D-period and D(002) versus macroscopic stress were taken as the unstrained (zero-stress) value for D-period and D(002), respectively. The effective fibril modulus ($E_f = d\sigma/d\varepsilon_f$) and effective mineral modulus ($E_m = d\sigma/d\varepsilon_m$) were defined as the slope of tissue-level stress σ versus fibril strain and mineral strain, respectively, from the elastic region of deformation.

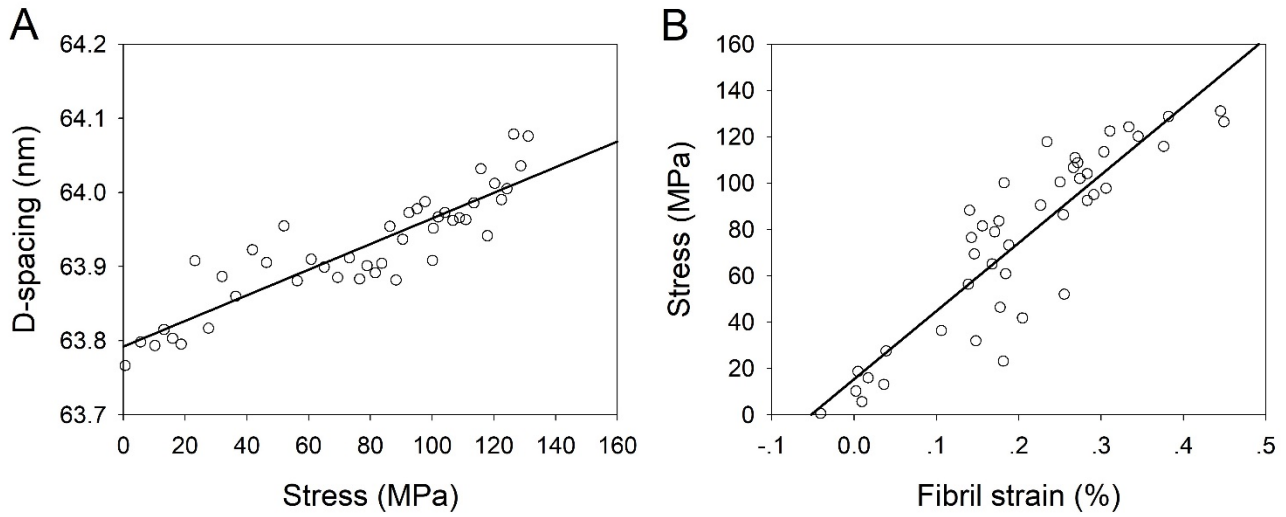

***Figure S3**: (A) D-spacing of collagen fibrils versus applied tissue stress; (B) applied tissue stress versus fibril strain. Black solid lines are linear regressions.*

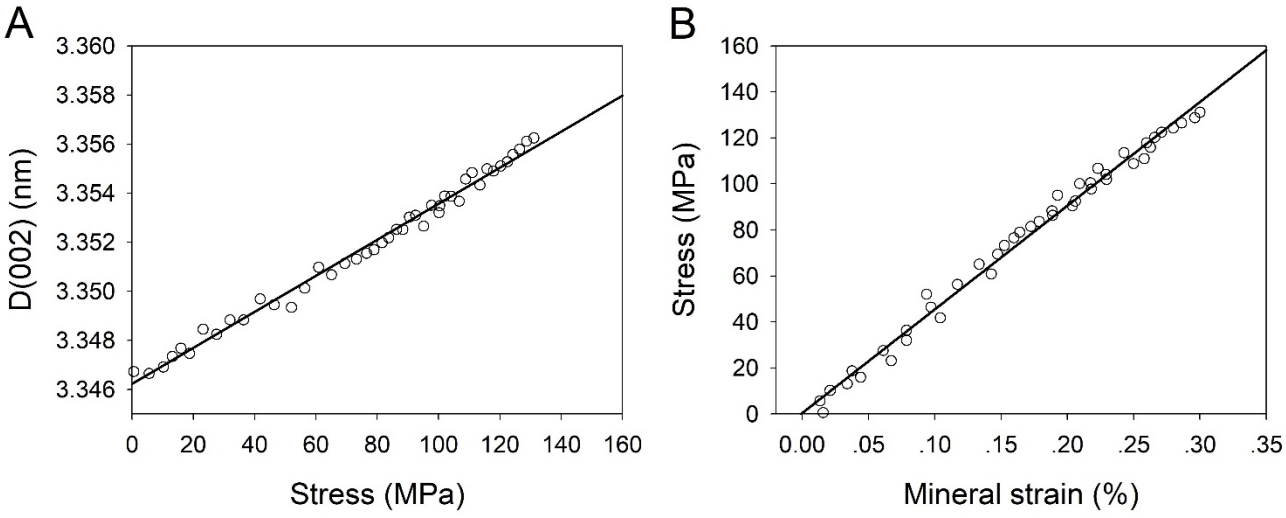

***Figure S4:** (A) (002) lattice spacing of apatite versus applied tissue stress; (B) applied tissue stress versus mineral strain. Black solid lines are linear regressions.*

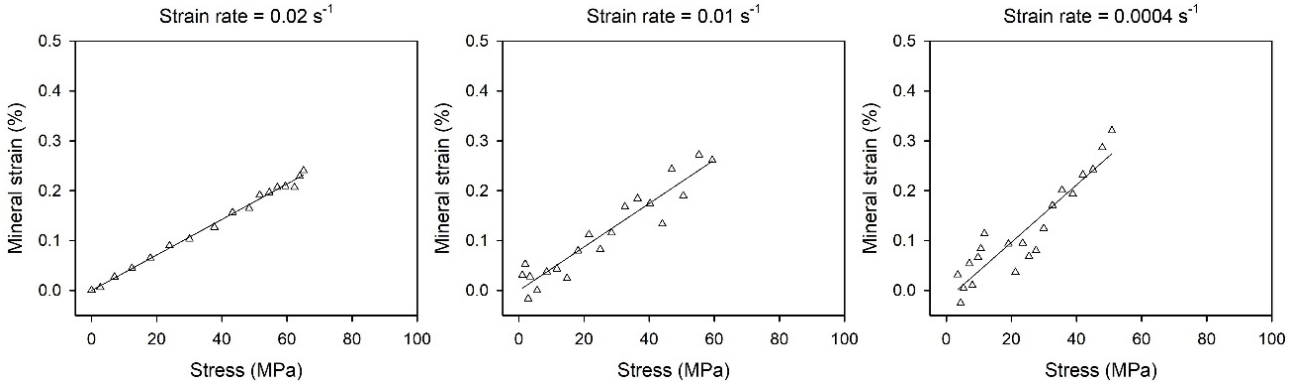

Figure S5: *Typical mineral strain versus stress curves for GIOP samples tested at three different strain rates.*

Figure S6 shows the simultaneous nonlinear fitting of the experimental effective fibrillar and mineral moduli that was performed in *Matlab.*

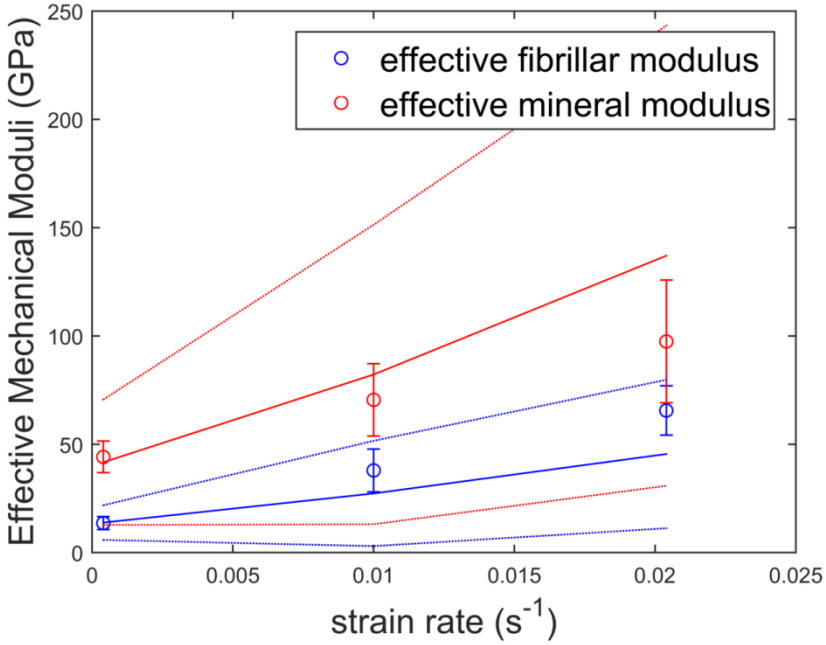

Figure S6: *Results from the three-parameter fitting process for the wild-type bone (**Section 2.8.1: Analytical Relations**). The experimental data was fitted by the numerical model (solid curves). The dotted curves show the 95% confidence interval. The output of the fit was: $c = 3.4\times10^{13}$ GPa.s, $d = 1.19$ (no units) and $\varphi_{EM} = 0.08$.*

Fibrillar mechanics and structure-function relations:

Assuming each sub-lamella to be orthotropic, the longitudinal and transverse Young's moduli and the shear modulus were determined by a combination of different variants of rules of mixtures. The longitudinal Young's modulus (E_1) was taken as the axial fibril modulus. This fibril modulus is derived from a staggered arrangement of mineral platelets in a collagen matrix [1-3] and depends on intrafibrillar mineral volume fraction, mineral platelet aspect ratio, and Young's moduli of collagen and mineral. Secondly, for the transverse modulus (E_2) and shear modulus (G_{12}) of the lamella, a Reuss (iso-stress) rule of mixtures was adopted [4, 5]. Finally, a Voigt (iso-strain) rule of mixtures was employed to calculate homogenized Poisson's ratios (ν_{12}).

Fibrils to mineral load transfer:

In order to estimate the longitudinal modulus of the fibrils a rule of mixture based on the Jager-Fratzl model was used [1] **(Equation S2).** Here, the difference with a standard Voigt rule is the presence of a *k*-factor at the denominator of the first term. This factor, reported in **Equation S6,** depends on the aspect ratio of mineral particles, on the Young's modulus of both the mineral and the collagen content and on the mineral volume fraction. The *k*-factor corresponds to the ratio between the effective mineral and the fibrillar moduli providing an estimation of how much of the strain is transferred from the fibrils to the intrafibrillar mineral platelets. Furthermore, the Jager-Fratzl is based on the assumption that mineral platelets and fibrils are parallel to each other. While for the wild-type bone we found that the *k*-factor resulting from the model was very similar to the experimental ratio between effective mineral modulus and effective fibrillar modulus, for the GIOP bone the two values were quite different. Therefore, assuming that in the GIOP bone mineral particles are not fully parallel to the longitudinal axis of the fibril, we implemented a parametric study imposing three values of *k* (1.7, 1.6, 1.58).

Analytical expressions for elastic moduli:

The main equations used for the calculation of the elastic moduli of a single sub-lamella are listed below. :

$$G_{m/c/EM} = \frac{E_{m/c}}{2\left(1+\nu_{m/c}\right)} \qquad (S1)$$

$$E_1 = \frac{E_m \varphi_m}{k} + \varphi_c E_c + \varphi_{EM} c\dot{\varepsilon}^d \qquad (S2)$$

$$E_2 = \frac{E_m E_c c\dot{\varepsilon}^d}{(\varphi_m E_c c\dot{\varepsilon}^d) + (\varphi_c E_m c\dot{\varepsilon}^d) + (\varphi_{EM} E_c E_m)} \qquad (S3)$$

$$G_{12} = \frac{G_m G_c G_{EM}}{(\varphi_m G_c G_{EM}) + (\varphi_c G_m G_{EM}) + (\varphi_{EM} G_m G_c)} \qquad (S4)$$

$$\nu_{12} = \varphi_m \nu_m + \varphi_c \nu_c + \varphi_{EM} \nu_{EM} \qquad (S5)$$

$$k = 1 + \left(\frac{4}{AR^2} \frac{1-\varphi_m}{\varphi_m} \frac{E_m}{\gamma_c E_c}\right) \qquad (S6)$$

In the equations above, φ_m is the mineral volume fraction, E is the Young's modulus, G is the shear modulus and ν is the Poisson's ratio. The subscript 1 indicates the longitudinal direction of sub-lamellae/fibrils while the subscript 2 the transverse direction. The subscripts m, c and EM indicate respectively the mineral, collagen and extrafibrillar matrix contents. The aspect ratio of the mineral platelet is AR while γ_c is a constant coefficient equal to 0.4. The symbol '/' indicates that **Equation S1** can be used for the shear modulus of the mineral, collagen and extrafibrillar matrix contents (under the assumption of basic isotropic material).

The material and geometrical properties used as input of the FE simulations are listed in **Table S2.**

Table S2: Geometrical and materials properties adopted for the FE simulations.

<table>
<tr><th></th><th>Wild-type bone</th><th>GIOP bone</th></tr>
<tr><td>Young's modulus of extrafibrillar matrix (GPa)</td><td>
<table>
<tr><th></th><th>Extrafibrillar matrix</th></tr>
<tr><td>low s.r.</td><td>3.5</td></tr>
<tr><td>medium s.r.</td><td>159.0</td></tr>
<tr><td>high</td><td>370.0</td></tr>
</table>
</td><td>
<table>
<tr><th></th><th>k = 1.58</th><th>k = 1.6</th><th>k = 1.7</th></tr>
<tr><td>low s.r.</td><td>163.8</td><td>107.6</td><td>53.0</td></tr>
<tr><td>medium s.r.</td><td>160.8</td><td>105.7</td><td>52.3</td></tr>
<tr><td>high</td><td>160.1</td><td>105.3</td><td>52.1</td></tr>
</table>
</td></tr>
<tr><td>Young's modulus of fibril (GPa)</td><td>$(E_m \times \frac{\varphi_m}{1-\varphi_{EM}}) + (E_c \times \frac{\varphi_c}{1-\varphi_{EM}}) =$
$= (100 \times 0.402) + (2.5 \times 0.598) =$
$= 41.7$ (GPa)</td><td>
<table>
<tr><th>k = 1.58</th><th>k = 1.6</th><th>k = 1.7</th></tr>
<tr><td>39.7</td><td>37.8</td><td>32.8</td></tr>
</table>
</td></tr>
<tr><td>Poisson's ratio</td><td>Extrafibrillar matrix: 0.3
Fibril: 0.3</td><td>Extrafibrillar matrix: 0.3
Fibril: 0.3</td></tr>
<tr><td>Surface area (per unit thickness)</td><td>Fibril:
1 μm × 0.1 μm

Extrafibrillar matrix:
1.009 μm × 0.109 μm – 0.1 μm ~ 0.01 μm</td><td>Fibril:
1 μm × 100 nm

Extrafibrillar matrix (μm):
<table>
<tr><th>k = 1.58</th><th>k = 1.6</th><th>k = 1.7</th></tr>
<tr><td>~ 0.003</td><td>~ 0.006</td><td>~ 0.015</td></tr>
</table>
</td></tr>
</table>

Lamellar structure from angular SAXS intensity:

Plywood structural parameters: The experimental azimuthal intensity distribution of the meridional collagen SAXD peak (**Figure S2**) was used to determine the angular distribution of sub-lamellae in the model [6]. The thicknesses of differently oriented sub-lamellae (at 0°, ±5°, ±10°, ±15°, ±30°, ±45°, ±60°, ±75° and 90° [7]) were varied till the effective FWHM of the simulated lamella matched the experimental FWHM [6]. The average FWHM was found to be 72.3 ± 11.4° in wild bone, and 75.8 ± 5.5°. Therefore, the wild bone resulted in a plywood structure with 10% of sub-lamellae at 0°, 11% of sub-lamellae at 5°, 11% of sub-lamellae at 10°, 28% of sub-lamellae at 15°, 20% at ± 30°, 12% at ± 45°, 6% at ± 60° and 2% at 75°. GIOP bone, instead, resulted in a plywood structure with 10% of sub-lamellae at 0°, 10% of sub-lamellae at 5°, 10% of sub-lamellae at 10°, 26% of sub-lamellae at 15°, 20% at ± 30°, 12% at ± 45°, 8% at ± 60° and 4% at 75°.

Finite-element simulation of load-induced reorientation.

To simulate the load-induced reorientation of fibrils toward the loading axis, a method was used based on finite element simulations. The reorientation of a fibril embedded in an extrafibrillar matrix was determined (**Figure 3B**), assuming isotropic material properties (**Table S2**), by applying a uniform traction of 10 MPa to the top edge of the fibril and calculating angular reorientation from the horizontal and longitudinal displacements. The three Young's moduli of extrafibrillar matrix were input into the simulations. The degrees of freedom of the bottom edge of the system were all constrained while at the top edge a surface traction load of 10 MPa was applied (**Figure S7**). The results do not depend on the specific load used, due to the linear elastic nature of the simulation, which implies the ratio of fibril reorientation to fibril strain is load-independent. The reorientation angle is $\arctan\left(\frac{\Delta X}{\Delta Y}\right)$, where ΔX and ΔY are, respectively, the relative horizontal and longitudinal displacements between the mid-point of the bottom edge (point 'a' in **Figure 3B**) and the mid-point of the mid-section (point 'b' in **Figure 3B**). The reorientation calculated from the displacements of the mid-point was taken as an approximation of the average reorientation of the entire system.

To compare the reorientation with the (experimentally observable) reduction in FWHM of the SAXD I(χ) curves, the reorientation angles – over all sub-lamellae – calculated from FE simulations were input into **Equation S7** to calculate the change of FWHM ($\Delta FWHM$):

$$\Delta FWHM = \frac{\sum_{i=1}^{N} w_i(\alpha_i - \alpha_0)\delta\alpha_i}{FWHM_0} \qquad (S7)$$

In **Equation S7**, i denotes the index of the sublamella and N is the total number of sublamellae. w_i is the fraction of sub-lamellae initially at the angle α_i, $\delta\alpha_i$ is the reorientation angle of each sub-lamella, $FWHM_0$ is the initial FWHM of the Gaussian distribution representing the angular lamellar distribution of bone and α_0 is the center of this Gaussian distribution (0^o in our convention). The number of finite elements included in the model was achieved after a convergence test (4767 CPS4R; 4-node bilinear, reduced integration with hourglass control elements).

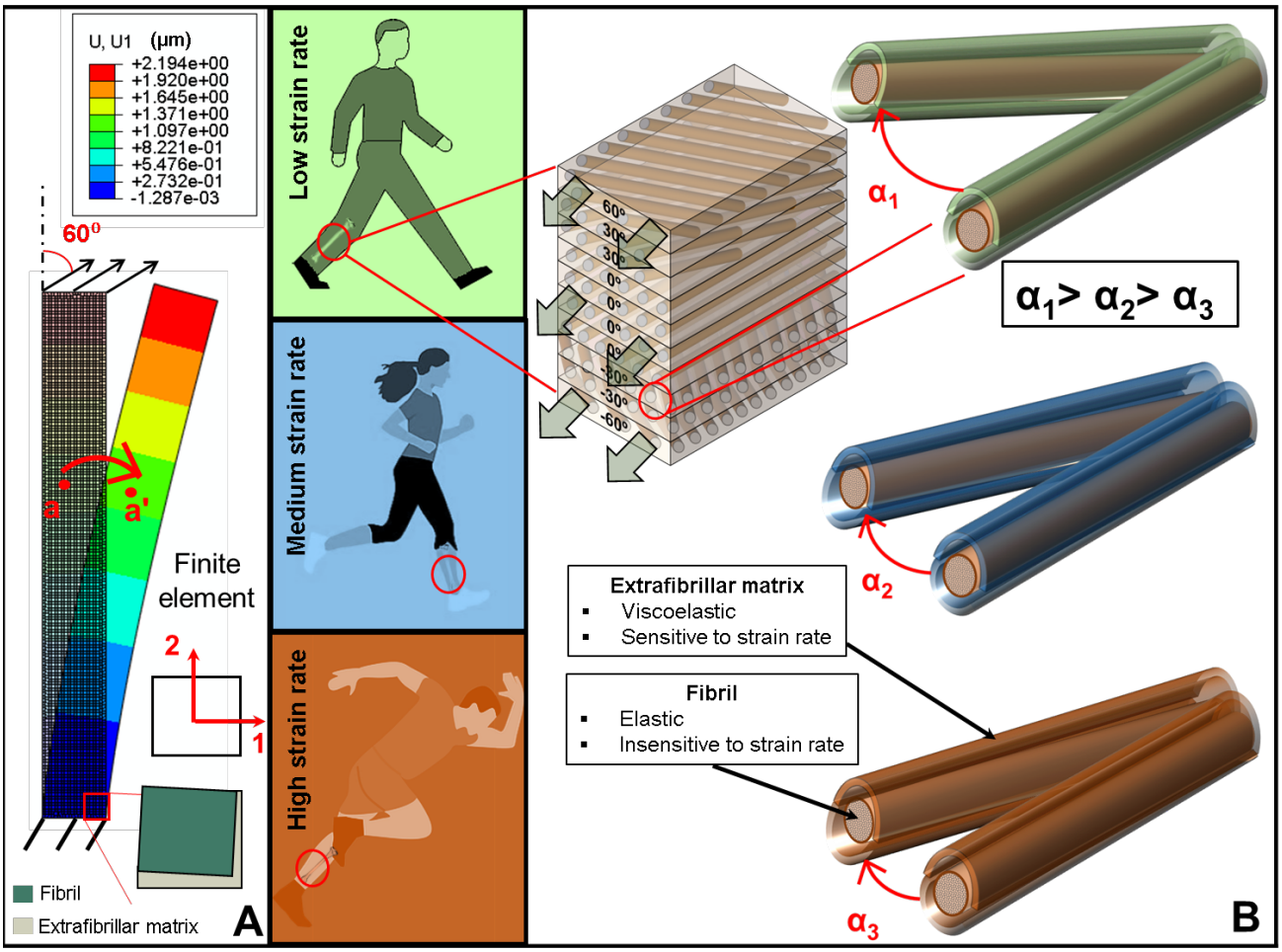

Figure S7: The effect of different strain rate levels on the reorientation phenomenon of fibrils in bone. *A) Example of FE model used to calculate the reorientation of the system 'fibril + extrafibrillar matrix' with its longitudinal axis oriented at 60° to the direction of the applied stress. The figure shows the deformation and reorientation of the system. Each represented colour is associated with a specific value of deformation of the finite elements. The magnified image shows the mechanism of deformation of the extrafibrillar matrix that accommodates the reorientation of the fibril. B) The viscoelastic extrafibrillar matrix is responsible for different levels of reorientation of fibrils in bone under different applied strain rate values. Indeed, our model assumes that the extrafibrillar matrix responds to an increasing applied strain rate with an increasing Young's modulus (stiffening effect) accommodating higher (for low strain rates) or lower (for high strain rates) reorientation of the elastic fibrils.*

References

[1] I. Jager, P. Fratzl, Mineralized collagen fibrils: A mechanical model with a staggered arrangement of mineral particles, Biophysical Journal 79(4) (2000) 1737-1746.

[2] H. Gupta, S. Krauss, M. Kerschnitzki, A. Karunaratne, J. Dunlop, A. Barber, P. Boesecke, S. Funari, P. Fratzl, Intrafibrillar plasticity through mineral/collagen sliding is the dominant mechanism for the extreme toughness of antler bone, Journal of the Mechanical Behavior of Biomedical Materials 28 (2013) 366-382.

[3] P. Fratzl, R. Weinkamer, Nature's hierarchical materials, Progress in Materials Science 52(8) (2007) 1263-1334.

[4] J.-M. Berthelot, F.F. Ling, Composite materials: mechanical behavior and structural analysis, Springer1999.

[5] D. Hull, T. Clyne, An introduction to composite materials, Cambridge university press1996.

[6] L. Xi, P. De Falco, E. Barbieri, A. Karunaratne, L. Bentley, C.T. Esapa, N.J. Terrill, S.D.M. Brown, R.D. Cox, G.R. Davis, N.M. Pugno, R.V. Thakker, H.S. Gupta, Bone matrix development in steroid-induced osteoporosis is associated with a consistently reduced fibrillar stiffness linked to altered bone mineral quality, Acta Biomater 76 (2018) 295-307.

[7] S. Weiner, W. Traub, H.D. Wagner, Lamellar bone: structure–function relations, Journal of structural biology 126(3) (1999) 241-255.